

Electromagnetic Proton Beam Instabilities in the Inner Heliosphere: Energy Transfer Rate, Radial Distribution, and Effective Excitation

WEN LIU,^{1,2} JINSONG ZHAO,^{1,2,3} HUASHENG XIE,^{4,5} YUHANG YAO,^{1,2} DEJIN WU,¹ AND L. C. LEE^{6,7}

¹*Key Laboratory of Planetary Sciences, Purple Mountain Observatory, Chinese Academy of Sciences, Nanjing 210023, People's Republic of China*

²*School of Astronomy and Space Science, University of Science and Technology of China, Hefei 230026, People's Republic of China*

³*Key Laboratory of Solar Activity, National Astronomical Observatories, Chinese Academy of Sciences, Beijing 100012, China*

⁴*Hebei Key Laboratory of Compact Fusion, Langfang 065001, People's Republic of China*

⁵*ENN Science and Technology Development Co., Ltd., Langfang 065001, People's Republic of China*

⁶*Institute of Earth Sciences, Academia Sinica, Taipei, 11529, Taiwan*

⁷*Space Science Institute, Macau University of Science and Technology, Macau, People's Republic of China*

(Accepted)

ABSTRACT

Differential flows among different ion species are often observed in the solar wind, and such ion differential flows can provide the free energy to drive Alfvén/ion-cyclotron and fast-magnetosonic/whistler instabilities. Previous works mainly focused on ion beam instability under the parameters representative of the solar wind nearby 1 au. In this paper we further study proton beam instability using the radial models of the magnetic field and plasma parameters in the inner heliosphere. We explore a comprehensive distribution of proton beam instability as functions of the heliocentric distance and the beam speed. We also perform a detailed analysis of the energy transfer between unstable waves and particles and quantify how much the free energy of the proton beam flows into unstable waves and other kinds of particle species (i.e., proton core, alpha particle, and electron). This work clarifies that both parallel and perpendicular electric fields are responsible for the excitation of oblique Alfvén/ion-cyclotron and oblique fast-magnetosonic/whistler instabilities. Moreover, this work proposes an effective growth length to estimate whether the instability is efficiently excited or not. It shows that oblique Alfvén/ion-cyclotron instability, oblique fast-magnetosonic/whistler instability, and oblique Alfvén/ion-beam instability can be efficiently driven by proton beams drifting at the speed $\sim 600 - 1300 \text{ km s}^{-1}$ in the solar atmosphere. In particular, oblique Alfvén/ion-cyclotron waves driven in the solar atmosphere can be significantly damped therein, leading to the solar corona heating. These results are helpful for understanding proton beam dynamics in the inner heliosphere and can be verified through in situ satellite measurements.

Keywords: Plasma physics (2089) — Space plasmas (1544) — Solar wind (1534)

1. INTRODUCTION

The proton velocity distribution in the solar wind usually consists of two components (Feldman et al. 1973, 1974; Marsch et al. 1982b): a more dense core and a secondary tenuous beam that drifts at a speed faster than the core. The proton beam component was firstly found by Feldman et al. (1973) from the IMP space-

crafts. Helios observations further identified the proton beam population arising from heliocentric distance 0.3–1 au (Marsch et al. 1982b). The statistical analysis for the Helios and Ulysses data sets have explored that the differential drift speed ΔV between the core and beam components is of the order of the local Alfvén speed V_A (Marsch & Livi 1987; Goldstein et al. 2000; Tu et al. 2004; Alterman et al. 2018; Āurovcová et al. 2019). The observed $\Delta V/V_A$ are normally less than the values predicted from proton beam instability (Marsch & Livi 1987; Goldstein et al. 2000). Consequently, proton beam instability is proposed to play a significant role in con-

straining the proton beam in the solar wind (Marsch & Livi 1987; Goldstein et al. 2000).

The proton beam provides one of free energies to drive the electromagnetic instabilities. Montgomery et al. (1975, 1976) firstly performed a comprehensive investigation of proton beam instability in a plasma containing proton core, proton beam, and electron components, and found that the proton beam induces three kinds of instabilities: oblique Alfvén/ion-cyclotron instability, oblique fast-magnetosonic/whistler instability, and parallel fast-magnetosonic/whistler instability. Daughton & Gary (1998) reconsidered proton beam instability, and identified the appearance of two kinds of oblique Alfvén/ion-cyclotron instabilities, i.e., Alfvén I occurring at comparatively short wavelengths (also see Winske & Omid 1992), and Alfvén II at comparatively longer wavelengths (also see Montgomery et al. 1975, 1976). Besides, the proton beam could drive parallel Alfvén/ion-cyclotron instability that have a speed threshold higher than that for parallel fast-magnetosonic/whistler instability (e.g., Gary 1991; Liu et al. 2019). Among these instabilities, parallel fast-magnetosonic/whistler and Alfvén I instabilities are the two strongest instabilities under plasma parameters representative of 1 au solar wind, and they are thought of as the candidates constraining the proton beam therein (Daughton & Gary 1998; Daughton et al. 1999).

In contrast to studies of proton beam instability in the vicinity of the solar wind at 1 au, there are a few works that have focused on such instability in the region close to the Sun. Recently, Liu et al. (2019) proposed that parallel Alfvén/ion-cyclotron and fast-magnetosonic/whistler instabilities can be driven by the proton beam in the solar coronal holes. Using the Parker Solar Probe (PSP) measurements, Verniero et al. (2020) reported observations of the simultaneous occurrence of proton beams and ion-scale waves at heliocentric distances of about $36R_S$, and identified that the observed waves are locally driven by proton beams on the basis of the instability analysis. Bowen et al. (2020) showed that ion-scale waves are observed 30% – 50% radial field intervals in the first encounter of PSP. Moreover, in comparison to the proton beam speed comparable to V_A in the solar wind nearby 1 au, proton beams are at times seen by PSP with relative speeds $\gtrsim 1.5V_A$ (Klein et al. 2021). Since PSP will measure the ion velocity distribution and electromagnetic fields down to the heliocentric distance at $9.8R_S$, it provides a unique opportunity to identify the excitation of proton beam instability in the solar atmosphere. Consequently, this paper plans to investigate proton beam instability in both the solar atmosphere and the solar wind.

In this paper, different from previous works that use parameters representative of one location in the solar wind, we study the ion-scale proton beam instability under parameters radially distributed in the heliocentric distance from $3 - 215R_S$. This study explores the nature of four typical instabilities, i.e., oblique Alfvén/ion-cyclotron instability, oblique fast-magnetosonic/whistler instability, oblique Alfvén/ion-beam instability, and parallel fast-magnetosonic/whistler instability, in the inner heliosphere. In particular, this study recognizes that the Alfvén I instability proposed by Daughton & Gary (1998) comes from the coupling between the Alfvén/alpha-cyclotron mode and the Alfvén/ion-beam mode. Also, this study explores the excitation mechanism of each kind of instability using the energy transfer rate between unstable waves and particles in both the parallel and perpendicular directions with respect to the background magnetic field, which clearly shows how much the proton beam energy flows into unstable waves and other particle components in each kind of instability. Furthermore, this study presents the controlling parameter region of each proton beam instability and proposes that oblique Alfvén/ion-cyclotron, oblique fast-magnetosonic/whistler, and Alfvén/ion-beam instabilities could be driven by the proton beam with the drift speed $\sim 600 - 1300 \text{ km s}^{-1}$ in the solar atmosphere, which can be checked by PSP observations.

This paper is organized as follows. Section 2 introduces the theoretical model and plasma parameters. Section 3 analyzes the nature and excitation mechanism of four typical proton beam instabilities. Section 4 gives the radial distributions of proton beam instability in the inner heliosphere. Section 5 considers the effective excitation of the instability. Section 6 discusses the change in the plasma temperature during proton beam instability and shows the dependence of the instability on plasma parameters, such as the temperature anisotropy, the differential drift of alpha particles relative to protons, and the relative proton beam density. Lastly, our results are summarized in Section 7.

2. THEORETICAL MODEL AND PLASMA PARAMETERS

2.1. Theoretical Model

To study the wave dynamics in the weakly collisional solar wind plasma, we use the model consisting of Vlasov and Maxwell's equations, which yield the wave equation in Fourier space

$$\mathbf{k} \times (\mathbf{k} \times \mathbf{E}) + \frac{\omega^2}{c^2} \epsilon \cdot \mathbf{E}, \quad (1)$$

where $\epsilon = i\sigma/(\epsilon_0\omega) + \mathbf{I}$, ϵ_0 is the permittivity of free space, ϵ is the dielectric tensor, σ is the conductivity tensor, ω is the wave frequency, and \mathbf{E} is the wave electric field. The plasma wave eigenmodes correspond to solutions of Equation (1). Recently, a general dispersion relation solver named BO/PDRK for Equation (1) was developed by Xie & Xiao (2016) and Xie (2019), and this solver is useful performing a comprehensive study for ion and electron kinetic instabilities (Sun et al. 2019, 2020). In this paper we use BO/PDRK to give the wave dispersion relation in proton beam plasma.

One key problem in the kinetic instability study is the role of Landau and cyclotron resonances between unstable waves and particles on the instability excitation. Both Landau and cyclotron resonances can induce the free energy of particles flowing into plasma waves, resulting in wave amplification (e.g., Gary 1991). To estimate the contribution of Landau and cyclotron resonances, a popular method is to calculate the resonance factor $\eta_{sn} = (\omega - k_{\parallel}V_s - n\Omega_{cs})/\sqrt{2}k_{\parallel}V_{Ts}$ (e.g., Gary 1991), where V_s is the drift velocity along the background magnetic field \mathbf{B}_0 , $V_{Ts} \equiv \sqrt{T_s/m_s}$ is the thermal speed, $\Omega_{cs} \equiv q_s B_0/m_s$ is the cyclotron frequency, and “s” denotes the particle species. Normally, $|\eta_{s0}| \lesssim 2$ (or 3) indicates that the Landau resonance interaction is important in triggering instability; and $|\eta_{sn}(n \neq 0)| \lesssim 2$ (or 3) implies that the cyclotron resonance interaction is in favor of triggering instability. We note that the transit-time resonant interaction can also arise as $\eta_{s0} \sim 0$ (e.g., Stix 1992; Quataert 1998).

This study will use an alternative parameter, i.e., the energy transfer rate, to quantify wave-particle resonances on the instability excitation. We will calculate the energy transfer rate by using the plasma current \mathbf{J} and the wave electric field \mathbf{E} . The similar energy absorption/emission calculation has been proposed by previous works (e.g., Stix 1992; Quataert 1998; Howes et al. 2017; Klein et al. 2017, 2019, 2020; He et al. 2020). Once the wave frequency and wave electric field fluctuations are obtained from Equation (1), the plasma current is given by

$$\mathbf{J}_s = \sigma_s \cdot \mathbf{E}. \quad (2)$$

The energy transfer rate between the waves and particles can be quantified by

$$\Gamma_s = \frac{1}{4} (\mathbf{E} \cdot \mathbf{J}_s^* + \mathbf{E}^* \cdot \mathbf{J}_s), \quad (3)$$

which denotes the energy absorption/emission per unit of time, and per unit of volume. Γ_s can be further decomposed as contributions from the parallel and perpen-

dicular electric fields:

$$\Gamma_{s\parallel} = \frac{1}{4} (\mathbf{E}_{\parallel} \cdot \mathbf{J}_{s\parallel}^* + \mathbf{E}_{\parallel}^* \cdot \mathbf{J}_{s\parallel}), \quad (4)$$

and

$$\Gamma_{s\perp} = \frac{1}{4} (\mathbf{E}_{\perp} \cdot \mathbf{J}_{s\perp}^* + \mathbf{E}_{\perp}^* \cdot \mathbf{J}_{s\perp}). \quad (5)$$

The total energy transfer rate can be obtained by summing all particle energy transfer rates: $\Gamma_t = \sum_s \Gamma_s$, $\Gamma_{t\parallel} = \sum_s \Gamma_{s\parallel}$, and $\Gamma_{t\perp} = \sum_s \Gamma_{s\perp}$. Since Landau and cyclotron resonances are dependent on parallel and perpendicular electric field fluctuations, respectively, they can be quantitatively measured by using Γ_{\parallel} and Γ_{\perp} . When the energy transfer rate is smaller than zero, the energy transfers from particles into waves, leading to wave growth. While the energy transfer rate is larger than zero, the energy transfers from waves into particles, leading to wave damping.

In this study we use the following expressions to quantify the energy transfer between the waves and particles,

$$P_s = \frac{\Gamma_s}{W_{EB}}, \quad P_{s\parallel} = \frac{\Gamma_{s\parallel}}{W_{EB}}, \quad P_{s\perp} = \frac{\Gamma_{s\perp}}{W_{EB}}, \quad (6)$$

and

$$P_t = \sum_s P_s, \quad P_{t\parallel} = \sum_s P_{s\parallel}, \quad P_{t\perp} = \sum_s P_{s\perp}. \quad (7)$$

where $W_{EB} = \epsilon_0 |\mathbf{E}|^2/4 + |\mathbf{B}|^2/4\mu_0$ is the wave electromagnetic energy. These expressions quantify the energy absorption/emission per unit of time, per unit of volume, and per unit of wave electromagnetic energy. We note that a different definition for the energy transfer is proposed in previous studies (e.g., Quataert 1998), and the relation between these two expressions is discussed in Appendix A. One advantage of using these normalized rates is that due to $P_t/2 = -\gamma$ (see Appendix A), we can directly measure the contribution of each resonance effect on wave growth or damping. Here, γ represents the imaginary part of ω in which $\gamma > 0$ (or < 0) corresponds to wave growth (or damping). In addition, we use ω to calculate P_t , not the real part of ω , and the reason is that a complete plasma current is only obtained by using ω (see Equation 2).

Furthermore, we will decompose the energy transfer rate at different n , i.e., $P_s(n)$, and investigate the contribution of $n = 0$ and $n \neq 0$ resonances on wave growth or damping. Based on these energy transfer rates, we will give detailed analyses for the growth and damping mechanism in each proton beam instability in Section 3.

2.2. Magnetic Field and Plasma Parameters

PSP will measure plasma waves and particle velocity distributions in situ down to locations below $10R_S$

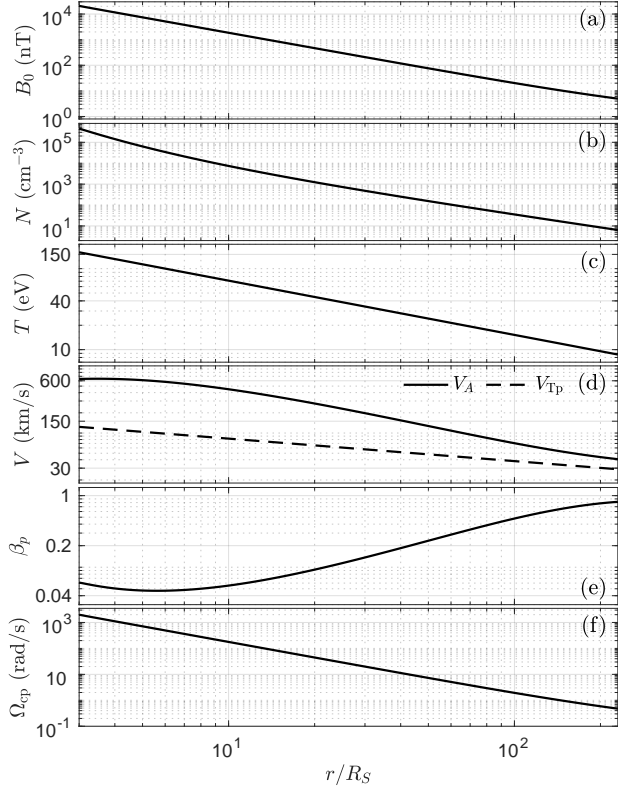


Figure 1. The radial distributions of the magnetic field strength and plasma parameters. (a) The magnetic field strength B_0 ; (b) the plasma number density N ; (c) the plasma temperature T ; (d) the Alfvén speed V_A (solid line), and proton thermal speed V_{Tp} (dashed line); (e) the plasma proton beta β_p defined as the ratio of the proton thermal pressure to magnetic pressure; and (f) the proton cyclotron frequency Ω_{cp} .

in the inner heliosphere. In order to provide a direct comparison between PSP observations and theoretical instability predictions, we use radial distributions of the magnetic field strength and plasma parameters at PSP orbits referring to Bale et al. (2016). The detailed fitting procedures are stated in Bale et al. (2016), and here we merely give the results.

The magnetic field strength is

$$B_0 = \frac{860R_S}{r} \sqrt{\left(\frac{215R_S}{r}\right)^2 + \left(\frac{405}{V_{sw}}\right)^2} \text{ (nT)}, \quad (8)$$

where r is the heliocentric distance, R_S is the solar radius, and the solar wind velocity is given as $V_{sw} = 430\sqrt{1 - \exp\left(-\frac{r/R_S - 2.8}{25}\right)}$ (km/s). The electron number density is (also see Sittler & Guhathakurta 1999)

$$N_e = N_0 \times \exp\left(\frac{3.67R_S}{r}\right) \left(\frac{R_S^2}{r^2} + \frac{4.9R_S^3}{r^3} + \frac{7.6R_S^4}{r^4} + \frac{6.0R_S^5}{r^5}\right) \quad (9)$$

with $N_0 = 3.26 \times 10^5 \text{ cm}^{-3}$, and the proton temperature is given by

$$T_p = \frac{T_0}{(r/R_S)^{0.6}}, \quad (10)$$

where $T_0 = 226.4 \text{ eV}$.

We consider a plasma containing four particle components, i.e., electrons “e”, proton core “pc”, proton beam “pb” and alpha particles “α”, and assume their velocity distribution functions following the drifting Maxwellian distribution, i.e., $f_s(v_{\parallel}, v_{\perp}) = \frac{N_s}{(\pi)^{3/2} (2T_s/m_s)^{3/2}} \exp\left[-\frac{(v_{\parallel} - V_s)^2 + v_{\perp}^2}{2T_s/m_s}\right]$, where m_s , N_s , T_s and V_s denote the mass, number density, temperature, and drift speed for each particle component “s”. We also consider the proton core frame, which is $V_{pc} = 0$. To better show the pure proton beam instability, we assume there is no differential drift between alpha particle and proton core components, i.e., $V_{\alpha} = 0$, while in fact, alpha particles are streaming faster than core protons in the solar wind (e.g., Marsch et al. 1982a; Alterman et al. 2018; Āurovcová et al. 2019). Moreover, we assume $N_{pb}V_{pb} - N_eV_e = 0$ to ensure a zero current condition. For the number density and temperature of each particle component, we use following values: $N_{pc} = 0.8N_e$, $N_{pb} = 0.1N_e$, and $N_{\alpha} = 0.05N_e$; and $T_{pc} = T_{pb} = T_{\alpha} = T_e$. The discussion of the dependence of the instability on the particle density and temperature will be given in Section 6.

The magnetic field strength and plasma parameters as a function of the heliocentric distance r are presented in Figure 1. Figure 1 also gives the radial distributions of the Alfvén speed V_A , the proton thermal speed V_{Tp} , the plasma proton beta β_p (the ratio of the proton thermal to magnetic pressure), and the proton cyclotron frequency Ω_{cp} . It should be emphasized that β_p is one important parameter affecting proton beam instability (Montgomery et al. 1976; Daughton & Gary 1998). From Figure 1, we see that β_p is smaller than 0.1 as $r \lesssim 20R_S$, and then β_p increases with r and is about 0.9 at $r = 155R_S$ (1 au).

2.3. Basic Wave Modes

For identifying which kind of the wave mode is unstable, this subsection introduces the basic wave modes in proton beam plasmas. The proton beam can considerably affect the dispersion relations of plasma waves (Liu et al. 2019), and an example is given in Figure 2, which presents all parallel and antiparallel

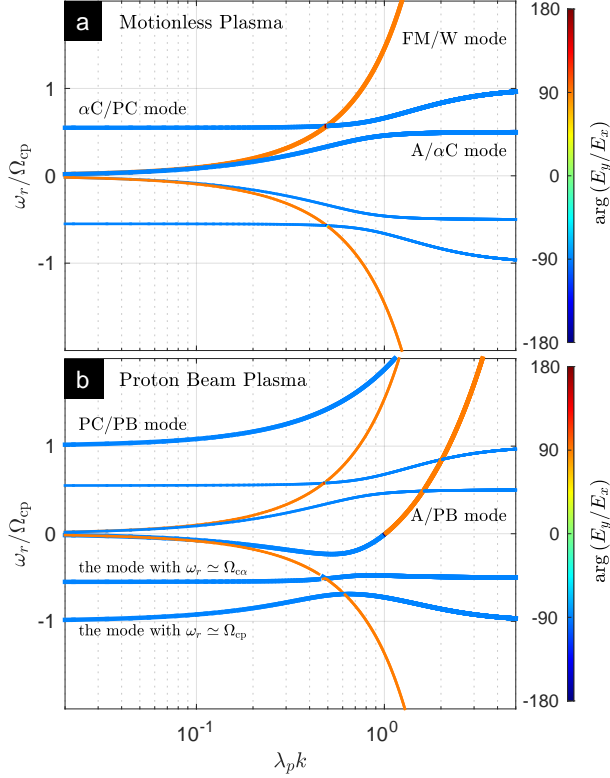


Figure 2. Parallel and antiparallel plasma waves in (a) a proton-alpha-electron plasma and (b) a plasma containing proton core, proton beam, alpha particle, and electron components. The argument of E_y/E_x is overlaid on the wave dispersion relations. Three wave modes correspond to the A/ α C (Alfvén/alpha-cyclotron) mode, the α C/PC (alpha-cyclotron/proton-cyclotron) mode, and the FM/W (fast-magnetosonic/whistler) mode in panel (a); and in panel (b) the wave modes significantly affected by the proton beam are the PC/PB (proton-cyclotron/proton-beam) mode, the A/PB (Alfvén/proton-beam) mode, the mode with the frequency near Ω_{ca} , and the mode with the frequency near Ω_{cp} .

low-frequency waves in a cold plasma. In an electron-proton-alpha particle plasma without any relative drifts between particle components, there are three kinds of wave modes below the electron cyclotron frequency: Alfvén/alpha-cyclotron mode, alpha-cyclotron/proton-cyclotron mode, and fast-magnetosonic/whistler mode (Figure 2a). When the plasma contains a proton beam with a drift speed $V_{pb} = V_A$ (Figure 2b), the coupling between the backward Alfvén/alpha-cyclotron mode and the proton beam mode results in the appearance of an Alfvén/proton-beam mode. The short-wavelength Alfvén/proton-beam mode wave becomes right-hand polarization and forward propagation due to the effect of the Doppler shift frequency $V_{pb}k_z$. Also, a new proton-cyclotron/proton-beam mode arises in the for-

ward propagation direction, and two left-hand polarized wave modes in the backward direction correspond to a mode with frequency near the alpha cyclotron frequency and a mode with frequency near the proton cyclotron frequency.

For the proton beam propagating against the background magnetic field, the basic wave modes are the same as that in Figure 2b, and only the difference is the wave direction. Therefore, this study considers the situation where the proton beam propagates along the background magnetic field.

3. FOUR TYPICAL PROTON BEAM INSTABILITIES

Using the magnetic field and plasma parameters stated in Subsection 2.2, we find there are four typical proton beam instabilities in the inner heliosphere. An example is given in Figure 3, which presents the $k - \theta$ distributions of these typical instabilities driven by proton beams with $V_{pb} = V_A$, $1.5V_A$, and $2.5V_A$ at $r = 10R_S$. The $V_{pb} = V_A$ proton beam drives an oblique Alfvén/ion-cyclotron instability, producing the left-hand polarized waves $\arg(E_y/E_x) = -90^\circ$, in which the maximum growth rate (marked by #1) occurs at $\theta \simeq 38^\circ$. The $V_{pb} = 1.5V_A$ beam results in an oblique fast-magnetosonic/whistler instability where the strongest excitation (marked by #2) occurs at $\theta \simeq 33^\circ$, and this instability generates the right-hand polarized waves with $\arg(E_y/E_x) = 90^\circ$. The proton beam with a large speed $V_{pb} = 2.5V_A$ triggers two kinds of instabilities: an oblique Alfvén/ion-beam instability with the local maximum growth rates (point #3 and #4) at $\theta \simeq 45^\circ$ and $\theta \simeq 73^\circ$, and a parallel fast-magnetosonic/whistler instability with the maximum growth rate at $\theta = 0^\circ$ (#5). The nature of each instability is further explored in Figures 4–13, which give a detailed analysis for each instability at its maximum growth rate.

3.1. Oblique Alfvén/ion-cyclotron instability

Figures 4a and 4b present the dispersion relations of all low-frequency waves and the growth rate of the unstable wave under $V_{pb} = V_A$ and $\theta = 38^\circ$ at $r = 10R_S$, respectively. Compared to the wave dispersion relations in Figure 2, it is evident that the unstable wave at point #1 is the Alfvén/alpha-cyclotron mode wave.

The energy transfer rates between unstable waves and particles are given in Figures 4c–4e. Through parallel electric field, the free energy of the proton beam is transferred into unstable waves. Simultaneously, the energy flows from unstable waves into the electron component; however, there is little energy transfer between unstable waves and the proton core (alpha particle) component

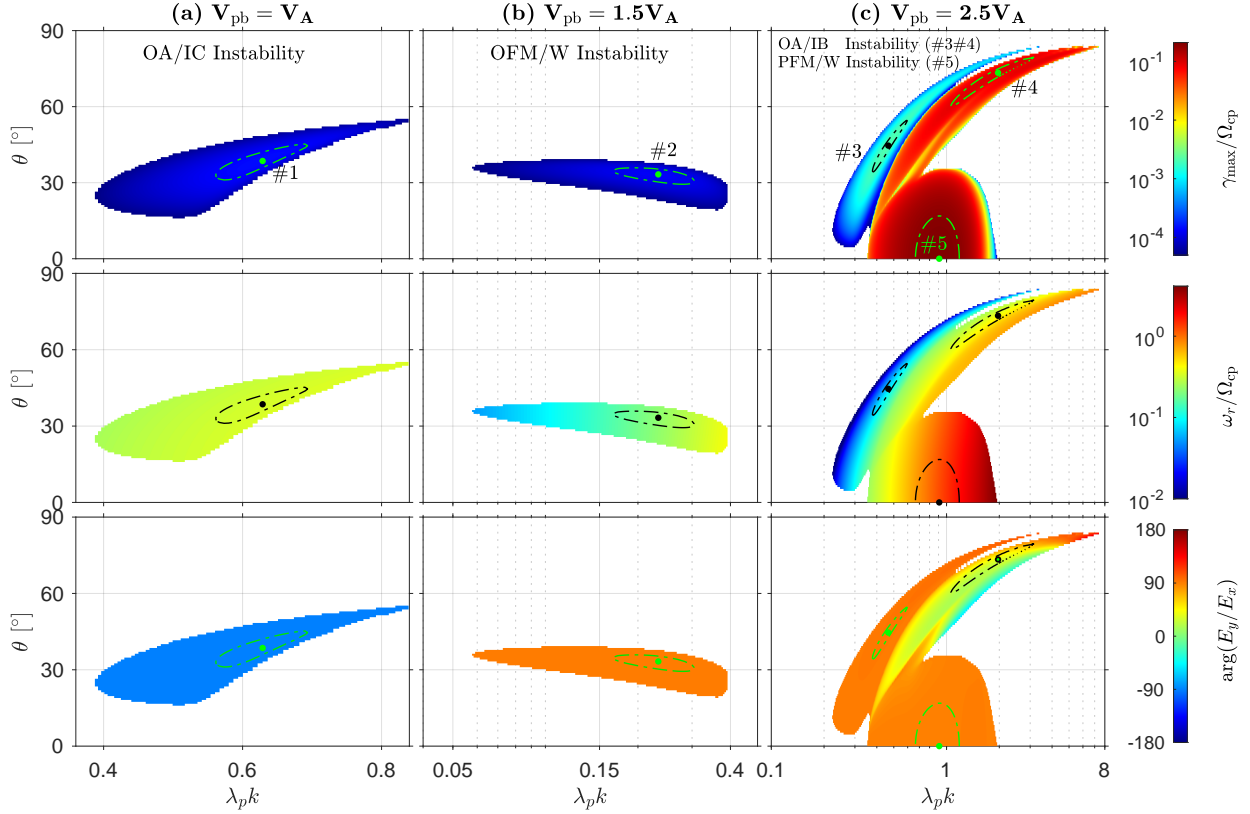


Figure 3. The $k - \theta$ distributions of four typical proton beam instabilities at $r = 10R_S$: (a) the OA/IC instability driven by the $V_{pb} = V_A$ proton beam; (b) the OFM/W instability driven by the $V_{pb} = 1.5V_A$ proton beam; and (c) the OA/IB instability and PFM/W instability driven by the $V_{pb} = 2.5V_A$ proton beam. (Top panels) the maximum growth rate, γ_{\max} ; (middle panels) the real frequency ω_r at γ_{\max} ; and (bottom panels) the argument of E_y/E_x at γ_{\max} . The circular points marked by #1, #2, #3, #4 and #5 denote local maximum growth rates, and the counter lines correspond to 0.9 times each local maximum growth rate. OA/IB = oblique Alfvén/ion-beam; OA/IC = oblique Alfvén/ion-cyclotron; OFM/W = oblique fast-magnetosonic/whistler; and PFM/W = parallel fast-magnetosonic/whistler.

in the parallel direction due to the parallel electric field. Since the total parallel energy transfer rate $P_{t\parallel}$ is mainly smaller than zero, the net energy flows into unstable waves in the parallel direction. On the other hand, both proton beam and electron components can release energy to unstable waves in the perpendicular direction due to the perpendicular electric field, whereas both the proton core and alpha particle components gain energy from unstable waves. Since $P_{t\perp} \lesssim 0$, the unstable waves gain the net energy from particles in the perpendicular direction. From Figure 4e which presents the energy transfer rate sum of both the parallel and perpendicular directions, we see that the free energy carried by the proton beam is nearly equally flowing into unstable waves and other particle components at the position of the strongest instability.

To understand the physical mechanisms driving parallel and perpendicular energy transfers, Figures 5 and 6 further show energy transfer rates at different n and typical diffusive particle flux paths in the $n = 0$ and $n = 1$

resonances, respectively. Since the oblique Alfvén/ion-cyclotron instability generates oblique left-hand polarized waves, these waves mainly interact with particles through $n = 0$ and $n = 1$ resonance (Figure 5; also see Verscharen & Chandran 2013).

A parallel electric field can induce strong Landau resonance interactions between unstable waves and $n = 0$ resonant particles (Figure 5a). Through comparing the wave dispersion relation and $n = 0$ resonance lines $\omega_r = (V_s \pm 2V_{Ts})k_{\parallel}$ and analyzing the diffusive particle flux path, we can estimate the effects of Landau resonance on unstable waves (Verscharen & Chandran 2013). The wave dispersion relation of the oblique Alfvén/ion-cyclotron wave, which can be approximately given as $\omega_{\text{OA/IC}} \sim V_A k_{\parallel}$, resides two resonance lines of the proton beam and electron components. This indicates that there are sufficient proton beam and electron particles taking part in Landau resonance interactions. For the proton beam population, $v_{ph} \leq v_{\parallel} \leq v_{ph} + 2V_{Tp}$ and $v_{ph} - 2V_{Tp} \leq v_{\parallel} \leq v_{ph}$ resonant protons may ex-

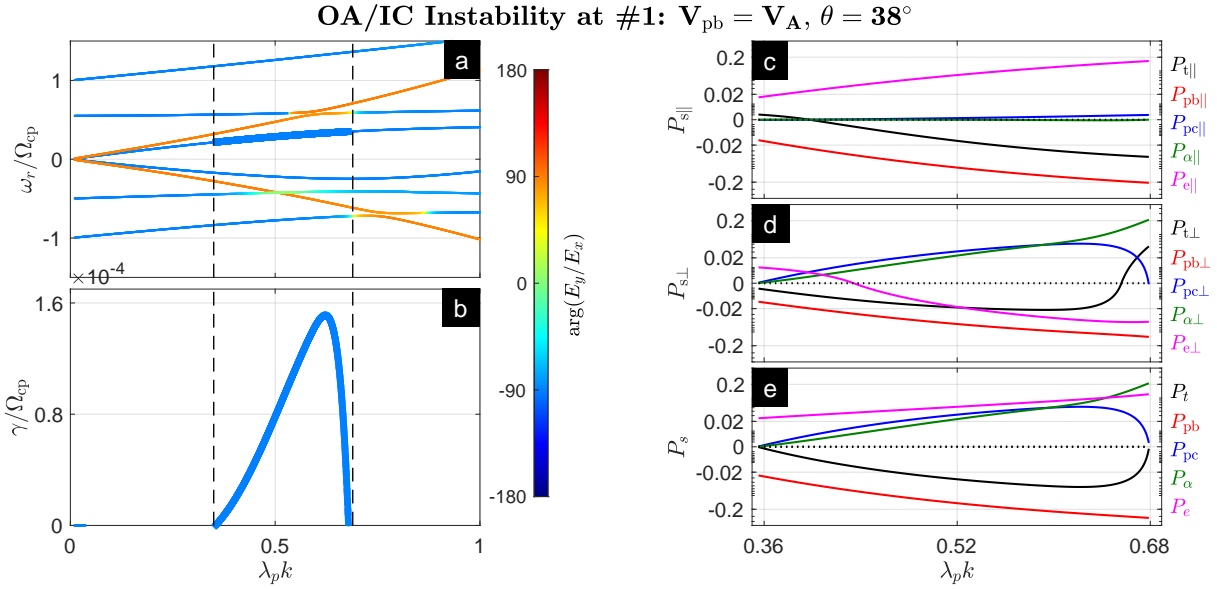


Figure 4. The OA/IC instability at point #1 labeled in Figure 3: (a) the dispersion relations of all low-frequency waves; (b) the growth rate of the unstable wave; (c) parallel energy transfer rates; (d) perpendicular energy transfer rates; and (e) total energy transfer rates. The argument of E_y/E_x is overlaid on the wave dispersion relation and growth rate. OA/IC = oblique Alfvén/ion-cyclotron.

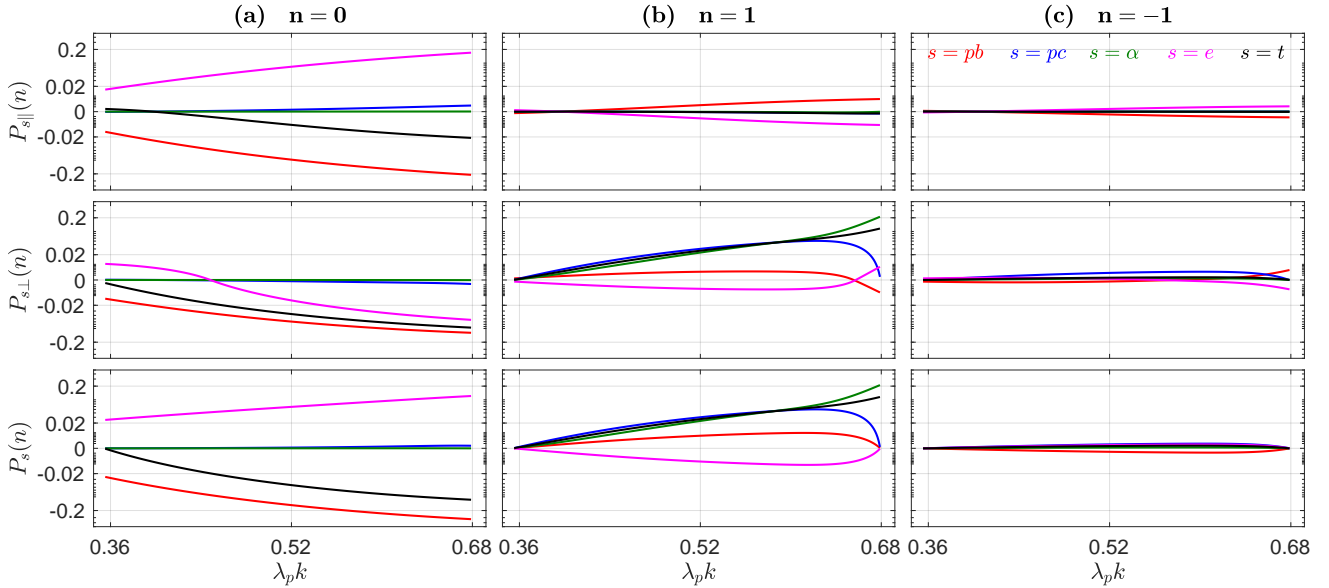


Figure 5. Energy transfer rates at different n in the oblique Alfvén/ion-cyclotron instability: (a) $n = 0$; (b) $n = 1$; and (c) $n = -1$. (Upper panels) parallel energy transfer rates; (middle panels) perpendicular energy transfer rates; and (bottom panels) total energy transfer rates.

perience different diffusion paths (Figure 6a) that are similar to diffusion paths for the Landau resonant alpha particle beam population proposed by Verscharen & Chandran (2013), and the total energy is flowing from these resonant protons into unstable waves, that is, $P_{pb||}(n = 0) < 0$. For the electron population, Landau interactions between resonant electrons with $v_{ph} - 2V_{Te} \leq v_{||} \leq v_{ph} + 2V_{Te}$ and unstable waves lead

to $P_{e||}(n = 0) > 0$. However, due to the wave dispersion relation highly deviating from two resonance lines of the proton core and alpha particle components, a few proton core and alpha particles experience Landau resonance interactions, and therefore $P_{pc||}(n = 0) \sim 0$ and $P_{\alpha||}(n = 0) \sim 0$.

The $n = 0$ resonant particles can suffer another kind of wave-particle interaction via a perpendicular electric

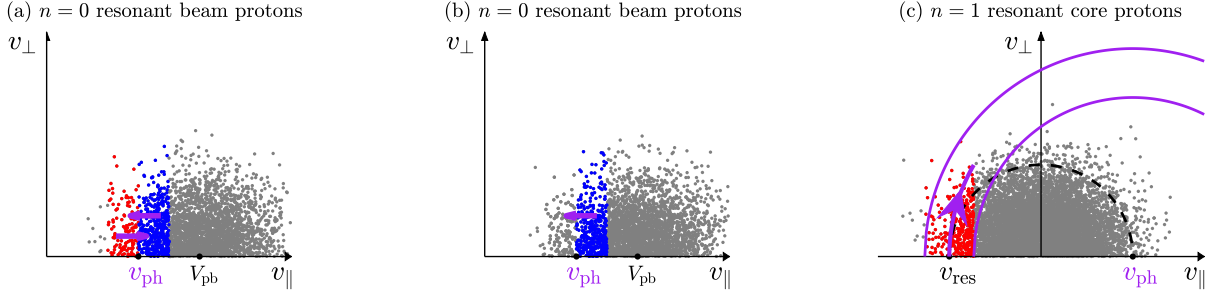


Figure 6. Diffusion paths in the oblique Alfvén/ion-cyclotron instability. (a) Landau interactions with $n = 0$ resonant beam protons, where red and blue points denote protons with $v_{ph} - 2V_{Tp} \leq v_{||} \leq v_{ph}$ and $v_{ph} \leq v_{||} \leq v_{ph} + 2V_{Tp}$, respectively. (b) Transit-time interactions with $n = 0$ resonant beam protons with $v_{ph} \leq v_{||} \leq v_{ph} + 2V_{Tp}$. (c) Cyclotron interactions with $n = 1$ resonant core protons with $v_{res} - 2V_{Tp} \leq v_{||} \leq v_{res} + 2V_{Tp}$. Blue (red) points represent particles diffusing into a region with smaller (larger) v . The black dashed and purple solid curves denote $v_{||}^2 + v_{\perp}^2 = C$ and $(v_{||} - v_{ph})^2 + v_{\perp}^2 = C$, respectively. The points are randomly sampled from the Maxwellian model for the proton beam or proton core population.

field, that is, transit-time resonant interaction (e.g., Stix 1992; Quataert 1998). Through the analysis for contributions of electric field components E_x and E_y on $P_{s\perp}(n = 0)$, we found that only E_y is responsible for $P_{s\perp}$ at $n = 0$ (not shown). Because E_y corresponds to B_z via Faraday's law, $n = 0$ resonant particles would be controlled by the motion equation $md_tv_{||} = -\mu\hat{\mathbf{b}} \cdot \nabla|\mathbf{B}|$, which will lead to resonant particles moving into smaller $v_{||}$ (Figure 6b; Stix 1992), where $\mu = mv_{\perp}^2/2B_0$ is the magnetic moment of particles, and $\hat{\mathbf{b}} = \mathbf{B}/B$. The transit-time resonant interaction leads $n = 0$ resonant beam protons losing energy, i.e., $P_{pb\perp}(n = 0) < 0$ (Figure 5a). Also, the transit-time resonant interaction can result in $n = 0$ resonant electrons losing energy in the large k region, i.e., $P_{e\perp}(n = 0) < 0$ (Figure 5a).

Furthermore, in order to satisfy $n = 1$ cyclotron resonance condition $\omega_r = k_{||}v_{res} + \Omega_{cs}$, resonant ions (electrons) should stream against (along) the background magnetic field. $n = 1$ resonant ions can absorb energy from unstable waves, and $n = 1$ resonant electrons can release energy into unstable waves (Figure 5b). However, the contribution to $P_{t\perp}(n = 1)$ mainly comes from the proton core and alpha particle components. Figure 6c gives a sketch for the cyclotron resonance mechanism of core protons and alpha particles. The quasilinear diffusion theory predicts that resonant core protons and alpha particles are scattered along the surface of a constant kinetic energy in the wave frame (Kennel & Engelmann 1966; Verscharen & Chandran 2013), i.e., $(v_{s||} - v_{ph})^2 + v_{s\perp}^2 = C$. When these resonant core protons and alpha particles move along the gradient in phase-space density (Figure 6c), they gain energy, as shown in Figure 5b, inducing wave damping.

It should be noted that a parallel electric field can lead to parallel energy transfer between unstable waves and

$n = 1$ resonant particles; however, this type interaction is weaker than the cyclotron resonant interaction.

3.2. Oblique fast-magnetosonic/whistler instability

Figures 7a and 7b show all stable and unstable waves at point #2, where $V_{pb} = 1.5V_A$ and $\theta = 33^\circ$. We clearly see that the unstable wave at point #2 corresponds to the fast-magnetosonic/whistler mode wave.

Figures 7c–7e present energy transfer rates between unstable waves and particles. These unstable waves absorb energy from the proton beam and mainly release energy toward the electron component in the parallel direction, in which the net energy flows from unstable waves into particles (Figure 7c). In the perpendicular direction, shown in Figure 7d, the net energy flowing into unstable waves approximates energy flowing into the electron component, and these two energy strengths are higher than that transferring into the proton core and alpha particle components. Consequently, the free energy lost from the proton beam flows into electrons, unstable waves, core protons, and alpha particles in sequence (Figure 7e).

Since oblique fast-magnetosonic/whistler waves have both parallel and perpendicular electric field fluctuations, these waves can interact with particles through $n = 0$ and $n = -1$ resonances, as shown in Figure 8, which gives energy transfer rates at different n .

For $n = 0$ resonant beam protons, their diffusive particle flux paths induced by a parallel electric field are the same as that illustrated in Figure 6a, and therefore these protons lose the kinetic energy. $n = 0$ resonant electrons gain energy from unstable waves through Landau resonance interactions. The perpendicular electric field induces energy flowing from $n = 0$ resonant beam protons into unstable waves in the perpendicular direction, in which the mechanism is the same as that illustrate in Figure 6b. However, different from $P_{e\perp}(n = 0) < 0$

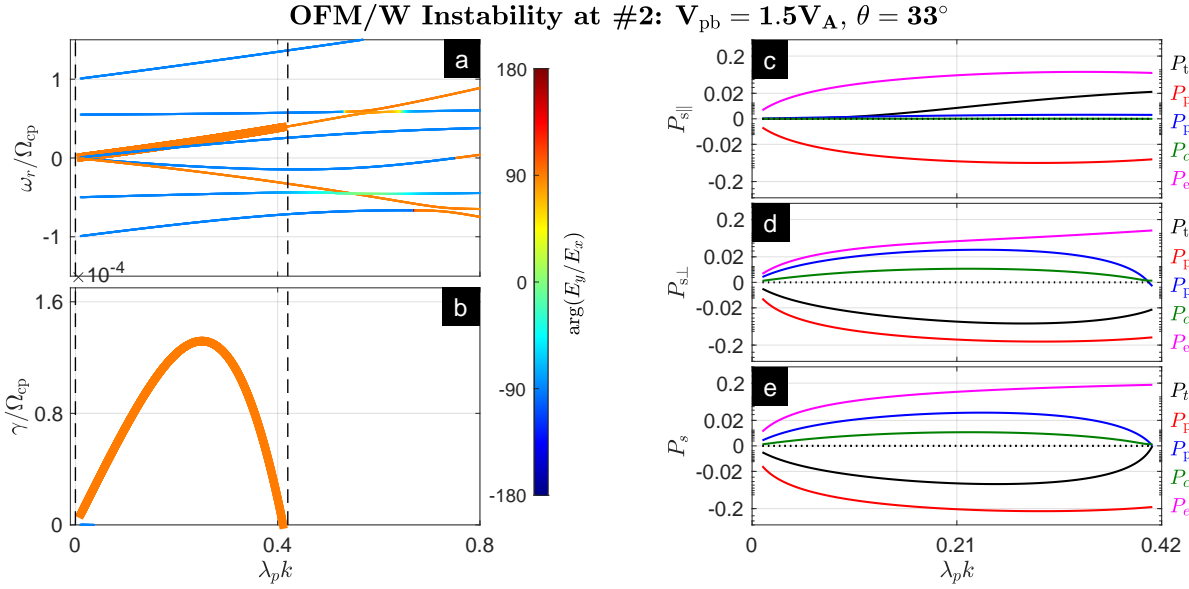


Figure 7. The OFM/W instability at point #2. The description of panels (a)-(e) are the same as those in Figure 4. OFM/W = oblique fast-magnetosonic/whistler.

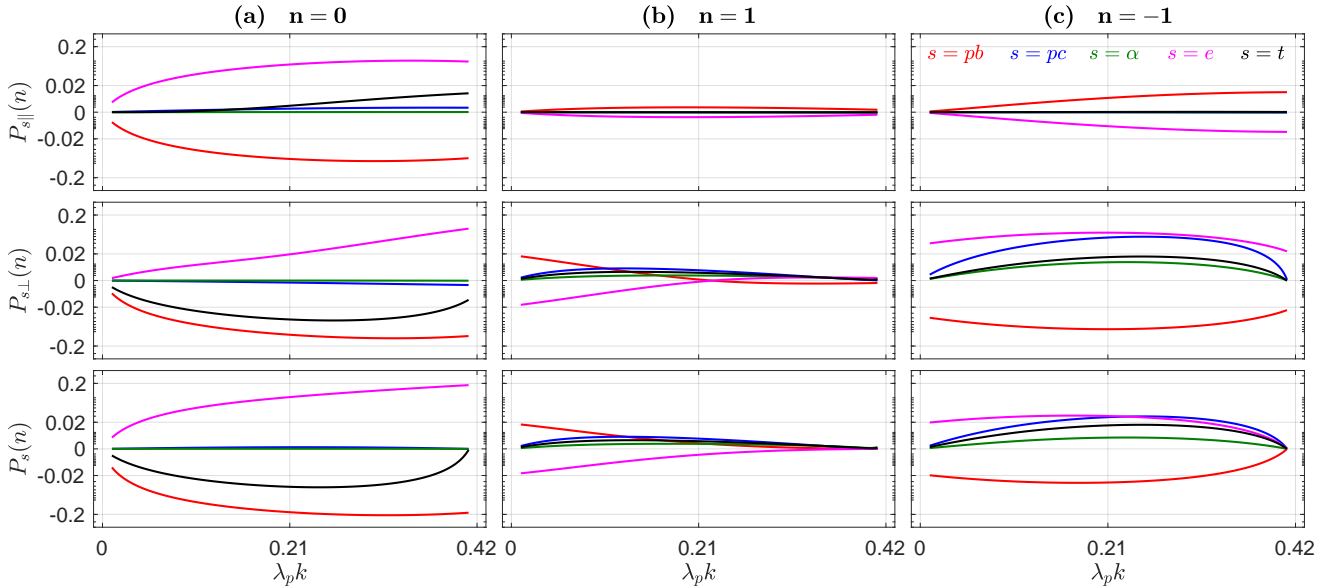


Figure 8. Energy transfer rates at different n in the oblique fast-magnetosonic/whistler instability at point #2: (a) $n = 0$; (b) $n = 1$; and (c) $n = -1$. (Upper panels) parallel energy transfer rates; (middle panels) perpendicular energy transfer rates; and (bottom panels) total energy transfer rates.

in Figure 5a, $n = 0$ resonant electrons obtain energy from unstable waves in the perpendicular direction, i.e., $P_{e\perp}(n = 0) > 0$ in Figure 8a. This indicates that $n = 0$ resonant electrons are scattered along the gradient in the electron phase-space density, that is, these electrons move to the region with higher kinetic energy.

Under the resonance condition of $\omega_r = k_{||}v_{res} - \Omega_{cs}$, $n = -1$ resonant particles correspond to forward streaming ions and backward streaming electrons. These particles should follow the diffusive particle flux paths il-

lustrated in Figure 9. As a consequence, beam protons lose the kinetic energy, and other particle components gain energy, resulting in $P_{pb}(n = -1) < 0$ and $P_{pc,\alpha,e}(n = -1) > 0$. In addition, because oblique fast-magnetosonic/whistler waves are not pure right-hand polarized mode, i.e., $E_x + iE_y = 0$ and $E_x - iE_y \neq 0$, there also exists weak $n = 1$ resonances, as shown in Figure 8.

3.3. Oblique Alfvén/ion-beam instability

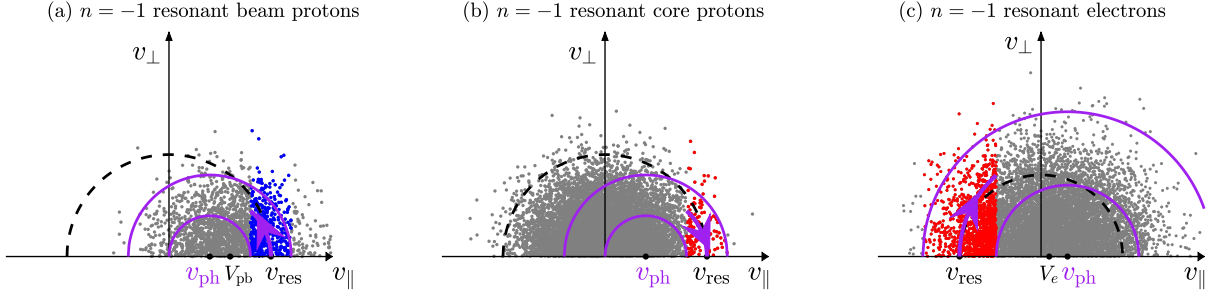


Figure 9. Diffusion paths in the oblique fast-magnetosonic/whistler instability. (a) Cyclotron interactions with $n = -1$ resonant beam protons with $v_{\text{res}} - 2V_{\text{Tp}} \leq v_{\parallel} \leq v_{\text{res}} + 2V_{\text{Tp}}$. (b) Cyclotron interactions with $n = -1$ resonant core protons with $v_{\text{res}} - 2V_{\text{Tp}} \leq v_{\parallel} \leq v_{\text{res}} + 2V_{\text{Tp}}$. (c) Cyclotron interactions with $n = -1$ resonant electrons with $v_{\text{res}} - 2V_{\text{Te}} \leq v_{\parallel} \leq v_{\text{res}} + 2V_{\text{Te}}$. Blue (red) points represent particles diffusing into a region with smaller (larger) v . The black dashed and purple solid curves denote $v_{\parallel}^2 + v_{\perp}^2 = C$ and $(v_{\parallel} - v_{\text{ph}})^2 + v_{\perp}^2 = C$, respectively. The points are randomly sampled from the Maxwellian model for the proton beam, proton core, or electron population.

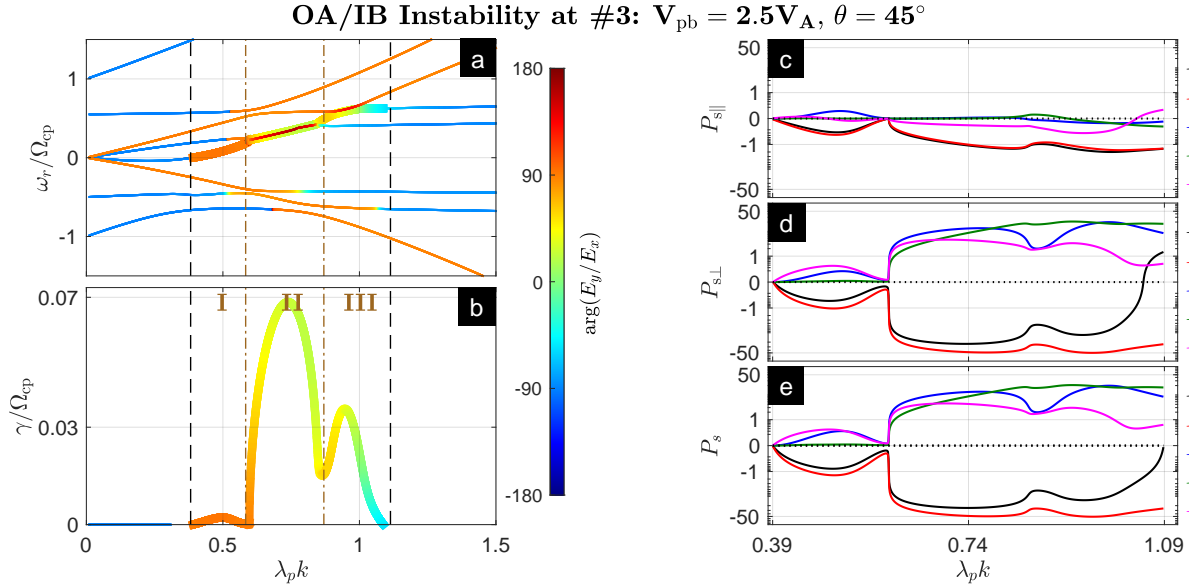


Figure 10. The OA/IB instability at point #3. The instability can be classified into three types labeled by I, II, and III. The description of panels (a)-(e) are the same as those in Figure 4. OA/IB = oblique Alfvén/ion-beam.

At points #3 and #4 in Figure 3c, the unstable wave corresponds to the oblique Alfvén/proton-beam mode wave, which is the reason why this instability is referred to as the oblique Alfvén/ion-beam instability. According to the dispersion relation and the growth rate of unstable waves in Figures 10 and 11, this instability is further classified into three types: Type-I, Type-II, and Type-III.

Here, we determine the basic features of these three type instabilities from Figures 10a–10b, which exhibit unstable Alfvén/ion-beam mode waves at $V_{\text{pb}} = 2.5V_A$ and $\theta = 45^\circ$. The unstable wave in Type-I instability corresponds to the low-frequency branch of the Alfvén/proton-beam wave, and this Type-I instability is the instability arising at #3 in Figure 3c. Differ-

ent from Type-I instability where the Alfvén/proton-beam wave decouples with the Alfvén/alpha-cyclotron wave, these two mode waves are coupled in Type-II instability. Type-II instability was previously named as Alfvén I instability by Daughton & Gary (1998). Besides, Type-III instability arises in the region where the oblique Alfvén/proton-beam mode wave meets the alpha-cyclotron mode wave.

Since Type-I is much weaker than Type-II and Type-III instabilities, energy transfer rates in Type-I instability are slower than that in other two instabilities. Here, we only discuss energy transfer rates in Type-II and Type-III instabilities. Figures 10c–10e show energy transfer rates of unstable Alfvén/ion-beam mode waves at $V_{\text{pb}} = 2.5V_A$ and $\theta = 45^\circ$. The energy transfer

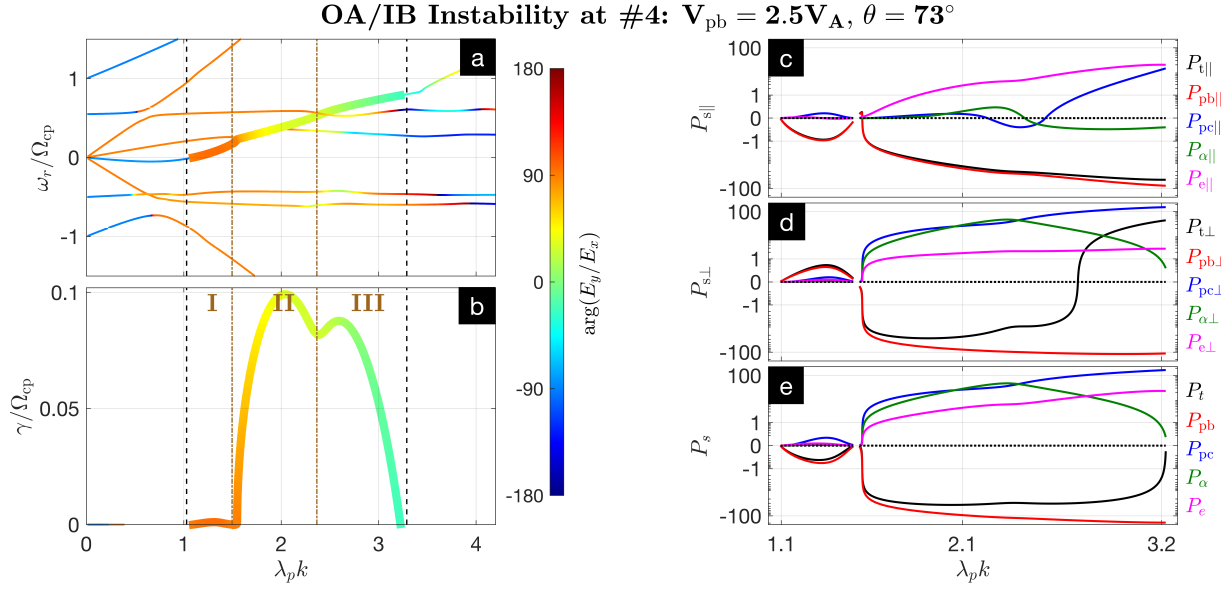


Figure 11. The OA/IB instability at point #4. The instability can be classified into three types labeled by I, II, and III. The description of panels (a)-(e) are the same as those in Figure 4. OA/IB = oblique Alfvén/ion-beam.

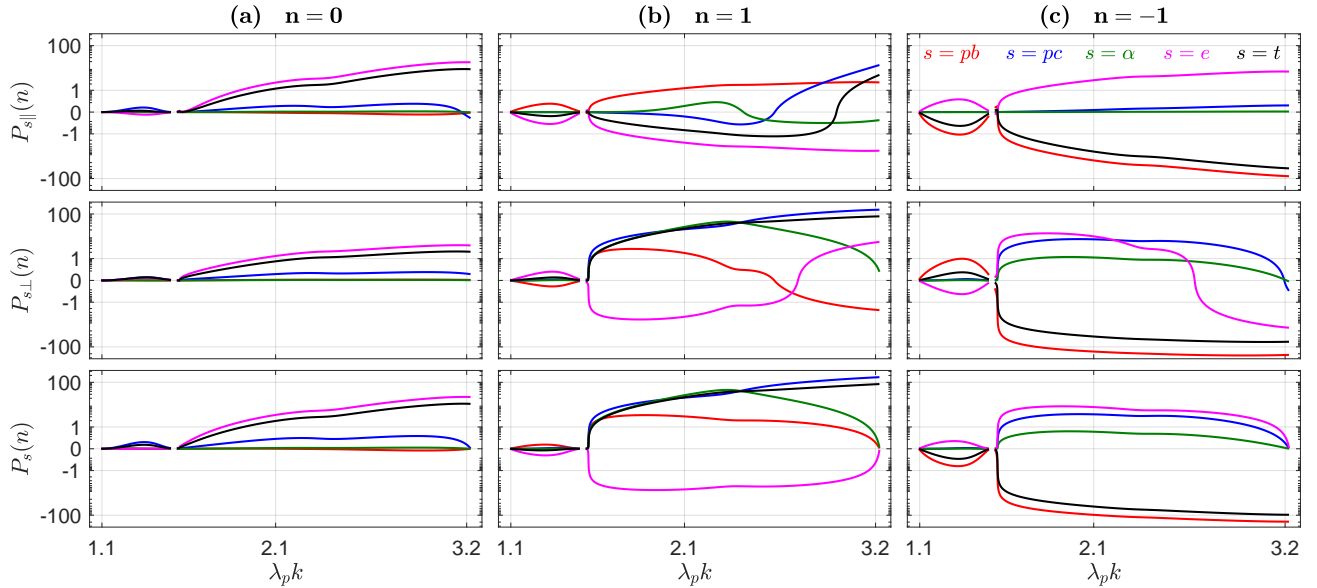


Figure 12. Energy transfer rates at different n in the oblique Alfvén/ion-beam instability at point #4: (a) $n=0$; (b) $n=1$; and (c) $n=-1$. (Upper panels) parallel energy transfer rates; (middle panels) perpendicular energy transfer rates; and (bottom panels) total energy transfer rates.

rate in the perpendicular direction dominates that in the parallel direction. In the perpendicular direction, beam protons lost energy in both Type-II and Type-III instabilities. However, there is an obvious difference between Type-II and Type-III instabilities, that is, core protons normally gain energy higher than alpha particles and electrons in Type-II instability, whereas alpha particles normally obtain energy approximating or slightly higher than core protons and electrons in Type-III instability. The reason for the latter is that Type-III instability ex-

cites alpha-cyclotron mode-like waves, which is in favor of the cyclotron resonance with alpha particles.

For the oblique Alfvén/ion-beam instability at $\theta = 73^\circ$ (see Figures 11a–11e), the distributions of Type-I and Type-II instabilities are similar to that at $\theta = 45^\circ$ in Figures 10a–10e. Here, Type-II instability is the instability arising at point #4 in Figure 3. Type-III instability at $\theta = 73^\circ$ is considerably different from that at $\theta = 45^\circ$, and this instability produces the oblique Alfvén/proton-beam wave with $\omega \gtrsim \Omega_{ca}$. In Type-III instability, the

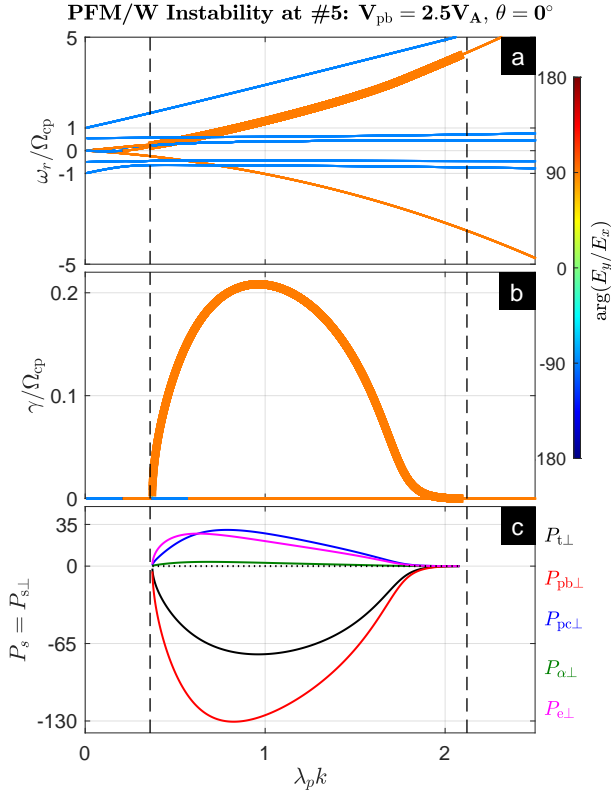


Figure 13. The PFM/W instability at point #5. The description of panels (a)-(c) are the same as those in Figure 4. PFM/W = parallel fast-magnetosonic/whistler.

energy lost from the proton beam is mainly flowing into core protons and alpha particles in the perpendicular direction, and unstable waves gain the net energy in both the parallel and perpendicular directions.

Furthermore, Figure 12 shows energy transfer rates at different n for unstable waves at $\theta = 73^\circ$. It is interesting to see that energy transfer rates associated with $n = 0$ resonant beam protons are nearly zero. Since the parallel phase velocity $\omega_{OA/IB}/k_{\parallel}$ of unstable Alfvén/ion-beam mode waves approximates the drift speed of the proton beam, the total number of the proton beam particles with $v_{\parallel} > \omega_{OA/IB}/k_{\parallel}$ is nearly the same as that with $v_{\parallel} < \omega_{OA/IB}/k_{\parallel}$, and this could lead to no net energy transfer between the waves and beam protons. Besides, because unstable waves are linearly polarized that means $E_x + iE_y \neq 0$ and $E_x - iE_y \neq 0$, both $n = 1$ and $n = -1$ resonances are important, and the corresponding resonant mechanisms are similar to the $n = 1$ resonance mechanisms shown in Figure 6 and the $n = -1$ resonance mechanisms shown in Figure 9.

3.4. Parallel fast-magnetosonic/whistler instability

Parallel fast-magnetosonic/whistler instability generates parallel fast-magnetosonic/whistler waves at point

#5, as shown in Figures 13a and 13b which present all low-frequency waves at $V_{pb} = 2.5V_A$ and $\theta = 0^\circ$. Since the parallel fast-magnetosonic/whistler wave is a pure right-hand mode wave, only the $n = -1$ resonance exists, and the energy transfer is limited to the perpendicular direction, as shown in Figure 13c. The diffusive particle flux paths of those resonant particles are the same as those given in Figure 9. As a result, beam protons lose energy, and other particle components gain energy.

4. RADIAL DISTRIBUTIONS

These four typical instabilities in Section 3 mainly control the evolution of the proton beam as it propagates outward from the Sun. In order to clearly explore controlling parameters of each instability, Figure 14 presents the $V_{pb} - \theta$ distributions of proton beam instability at three heliocentric distances: $r = 10R_S$, $55R_S$, and $100R_S$. Oblique Alfvén/ion-cyclotron instability appears at $r = 10R_S$ and disappears at $r = 55R_S$ and $r = 100R_S$. Oblique fast-magnetosonic/whistler instability is driven by proton beams with $V_{pb} \sim 1.3 - 1.8V_A$ at $r = 10R_S$ and by larger V_{pb} beams at larger heliocentric distances. To understand these differences at different r , we checked the energy transfer rate of the Alfvén/alpha-cyclotron wave under $V_{pb} = V_A$ and $\theta = 38^\circ$ and of the fast-magnetosonic/whistler wave under $V_{pb} = 1.5V_A$ and $\theta = 33^\circ$ at different heliocentric distances. For the oblique Alfvén/alpha-cyclotron wave, the Landau damping of core protons in the long-wavelength region and the cyclotron damping of alpha particles in the short-wavelength region significantly enhance at larger heliocentric distance. For the oblique fast-magnetosonic/whistler wave, Landau and cyclotron damping of core protons in the long-wavelength region and the cyclotron damping of electrons in the short-wavelength region considerably increase at larger heliocentric distance. Also, the energy transfer rate of the proton beam decreases with the heliocentric distance (this is due to the decrease of the proton beam speed). These effects result in different excitation behaviors of oblique Alfvén/ion-cyclotron and fast-magnetosonic/whistler instabilities at different heliocentric distances.

Figure 14 also shows that the normalized threshold V_{pb}/V_A of parallel fast-magnetosonic/whistler instability decreases with increasing heliocentric distance (with increasing β_p). However, the normalized threshold V_{pb}/V_A of oblique Alfvén/ion-beam instability increases with increasing heliocentric distance (with increasing β_p), and this instability can be always weaker than the parallel fast-magnetosonic/whistler instability at larger

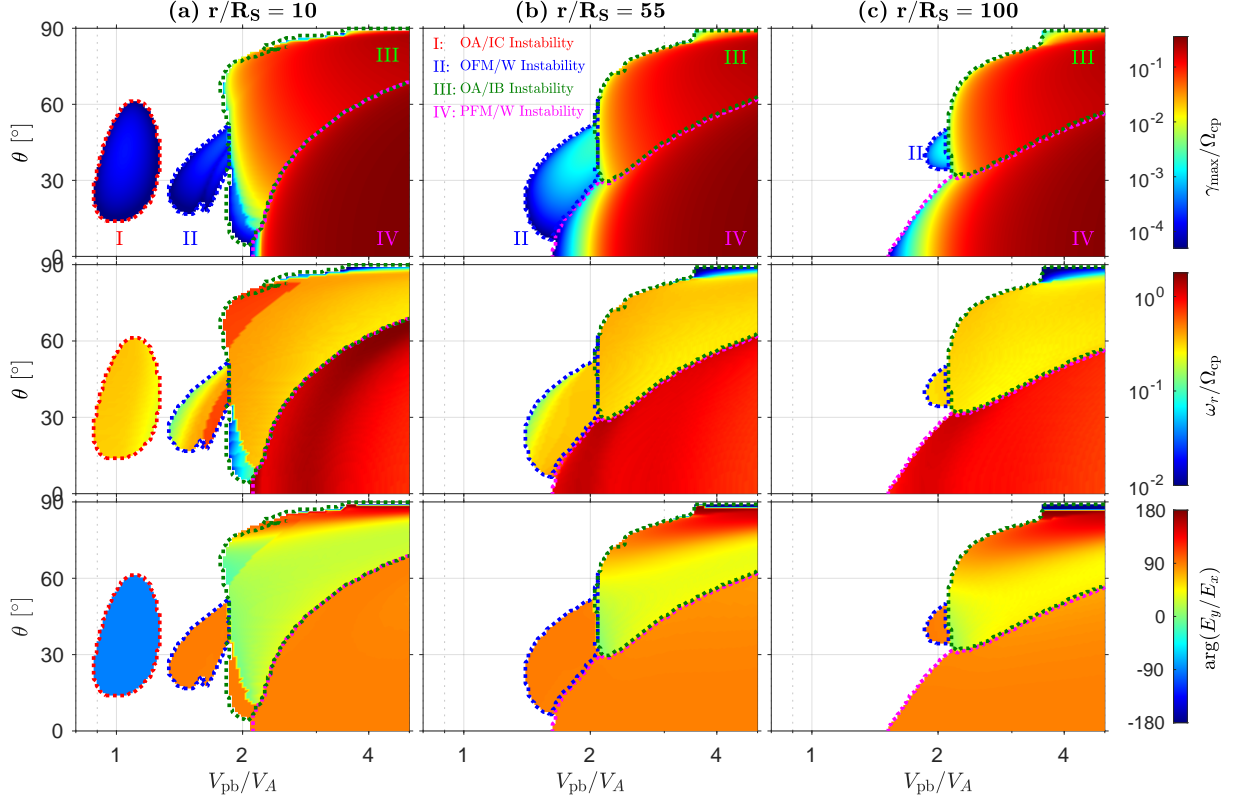


Figure 14. The $V_{pb} - \theta$ distributions of proton beam instability at (a) $r = 10R_S$, (b) $r = 55R_S$, and (c) $r = 100R_S$. (Top panels) The maximum growth rate, γ_{\max} ; (second panels) the real frequency ω_r at γ_{\max} ; and (bottom panels) the argument of E_y/E_x at γ_{\max} . The regions controlled by OA/IC, OFM/W, OA/IB, and PFM/W instabilities are denoted by I, II, III, and IV, respectively. OA/IB = oblique Alfvén/ion-beam; OA/IC = oblique Alfvén/ion-cyclotron; OFM/W = oblique fast-magnetosonic/whistler; and PFM/W = parallel fast-magnetosonic/whistler.

heliocentric distances. The β_p dependence in these two instabilities is consistent with the results given by Montgomery et al. (1976) and Daughton & Gary (1998).

The radial distribution of the ion-scale proton beam instability is shown in Figure 15, which gives the maximum growth rate γ_{\max} , and the real frequency ω_r , the argument angle of E_y/E_x , the absolute value of E_y/E_x , the wavenumber $\lambda_p k$ and the normal angle θ associated with γ_{\max} . Figure 15 exhibits different instabilities with different controlling regions. Oblique Alfvén/ion-cyclotron instability can control the region where $V_{pb} \sim 0.8 - 1.4V_A$ and $r \lesssim 30R_S$. Oblique fast-magnetosonic/whistler instability can arise in the region where $V_{pb} \sim 1.3 - 2.0V_A$ and $r \lesssim 60R_S$. Oblique Alfvén/ion-beam instability can exist in the region where $V_{pb} \sim 1.7 - 2.2V_A$ and $r \lesssim 30R_S$. Parallel fast-magnetosonic/whistler instability mainly controls the instability of the proton beam having $V_{pb} \sim 1.6 - 11V_A$. Besides, a parallel Alfvén/ion-cyclotron instability becomes dominant as the drifting speed of the proton beam is $V_{pb} \gtrsim 11V_A$. One of important theoretical predictions is that unstable oblique Alfvén/ion-cyclotron

and fast-magnetosonic/whistler waves can be produced by the proton beam in the solar atmosphere.

Moreover, Figure 16 gives the $r - V_{pb}$ distributions of the energy transfer rate. The basic features of the four typical instabilities are consistent with that explored in Section 3. For the fifth kind of instability, i.e., parallel Alfvén/ion-cyclotron instability, backward drifting electrons lose the kinetic energy that provides the free energy to amplify unstable waves, and the three ion components gain energy from unstable waves.

5. EFFECTIVE EXCITATION

Since the local Alfvén speed decreases with the heliocentric distance, when a proton beam is stable at small heliocentric distances, it will be destabilized at large heliocentric distances as its speed becomes larger than the local Alfvén speed therein. Hellinger & Trávníček (2011) have performed hybrid simulations to study the evolution of the proton beam in the expanding solar wind, and they indeed found a stable beam becomes unstable at large heliocentric distances. Since the energy carried by the proton beam is flowing into unstable waves and

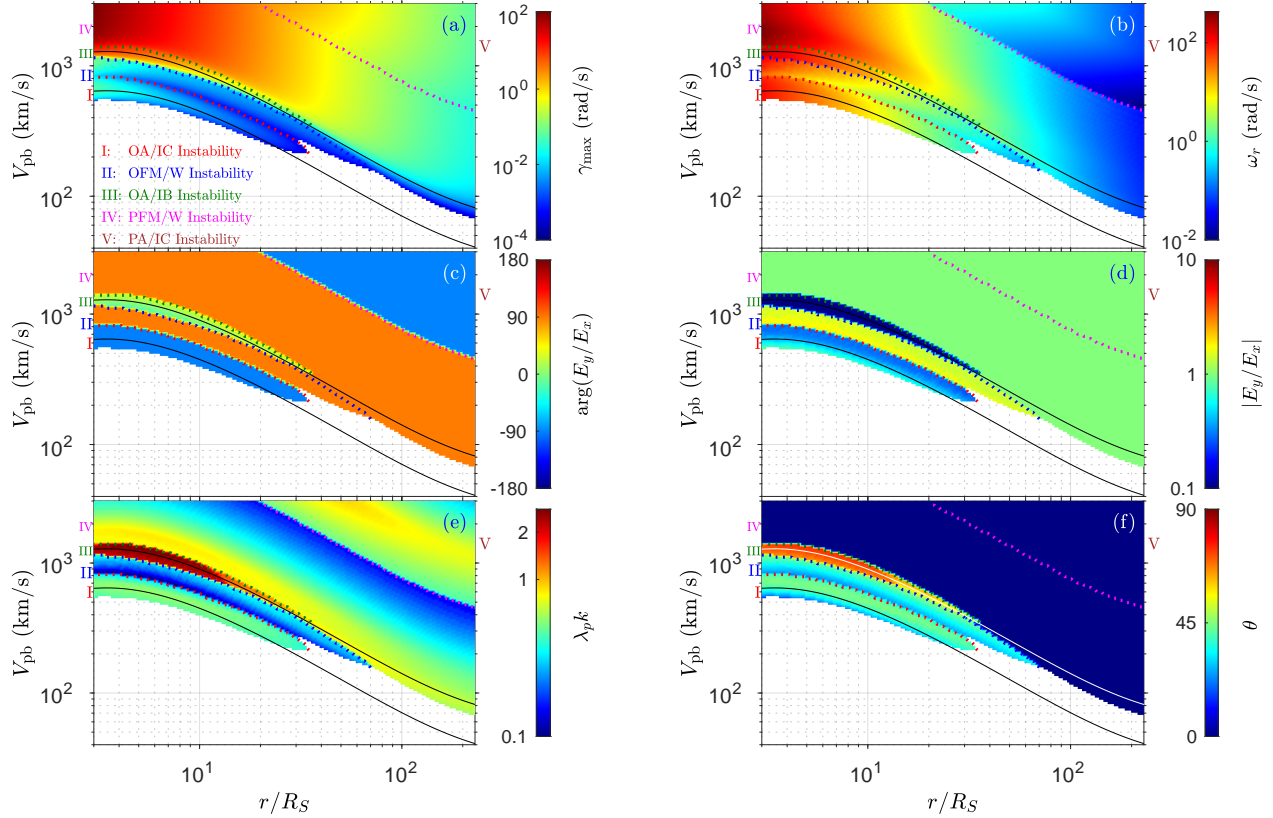


Figure 15. The $r - V_{pb}$ distributions of proton beam instability: (a) the maximum growth rate, γ_{\max} ; (b) the real frequency ω_r at γ_{\max} ; (c) the argument of E_y/E_x at γ_{\max} ; (d) the magnitude of E_y/E_x at γ_{\max} ; (e) the wavenumber k at γ_{\max} ; and (f) the wave normal angle θ at γ_{\max} . The regions controlled by OA/IC, OFM/W, OA/IB, PFM/W and PA/IC instabilities are denoted by I, II, III, IV and V, respectively. The boundary between two kinds of instabilities is denoted by dotted curves. Two solid curves represent $V_{pb} = V_A$ and $V_{pb} = 2V_A$, respectively. OA/IB = oblique Alfvén/ion-beam; OA/IC = oblique Alfvén/ion-cyclotron; OFM/W = oblique fast-magnetosonic/whistler; PA/IC=parallel Alfvén/ion-cyclotron; and PFM/W = parallel fast-magnetosonic/whistler.

other particle components during proton beam instability, the proton beam is slowed down. Proton beam instability can lead to an effective constraint on the beam speed once unstable waves are considerably growing during a short time.

To qualitatively estimate the effective excitation of the instability, we propose a parameter defined as the growth length L_{grow} , which is the propagating distance of the proton beam during a period when unstable waves are linearly growing from a noise level to a considerable large amplitude. The growth length is expressed as

$$L_{\text{grow}} = \int_{t=t_{\text{ini}}}^{t=t_{\text{ini}}+T_{\text{eff}}} (V_{\text{sw}} + V_{\text{pb}}(t)) dt, \quad (11)$$

where T_{eff} denotes the effective growing time. The corresponding wave amplitude δB evolves as $\delta B = \delta B_{\text{ini}} \exp\left(\int_{t=t_{\text{ini}}}^{t=t_{\text{ini}}+T_{\text{eff}}} \gamma(t) dt\right)$ during T_{eff} , where δB_{ini} is the wave amplitude at a noise level. Consequently, L_{grow} can be obtained once one knows $V_{\text{pb}}(t)$ and T_{eff} , in which T_{eff} are given as $\delta B/\delta B_{\text{ini}}$ and $\gamma(t)$ are known.

Since the free energy of the proton beam is continuously decreasing during the linear growth stage of the instability, both $V_{\text{pb}}(t)$ and $\gamma(t)$ are decreasing. In principle, a quasi-linear theory should be used to proceed with a self-consistent treatment of the variables $V_{\text{pb}}(t)$, $\gamma(t)$, and $\delta B/\delta B_{\text{ini}}$. However, for performing a qualitative estimation, we consider a constant γ , and thus T_{eff} is given as $T_{\text{eff}} = \ln(\delta B/\delta B_{\text{ini}})/\gamma$. Assuming $\delta B/B_0 = 0.1$ and $\delta B_{\text{ini}}/B_0 = 10^{-5}$, we have $T_{\text{eff}} \simeq 9/\gamma$. On the other hand, we can also estimate T_{eff} through referring to the hybrid simulation results (Daughton et al. 1999), which exhibited that a transition from the linear growth stage to the nonlinear stage occurs at $\Omega_{\text{cp}} t \sim 60$ in parallel fast-magnetosonic/whistler instability and at $\Omega_{\text{cp}} t \sim 110$ in Alfvén I instability (oblique Alfvén/ion-beam instability). Considering the initial growth rate $\gamma = 0.1\Omega_{\text{cp}}$ (Daughton et al. 1999), T_{eff} is nearly $10/\gamma$.

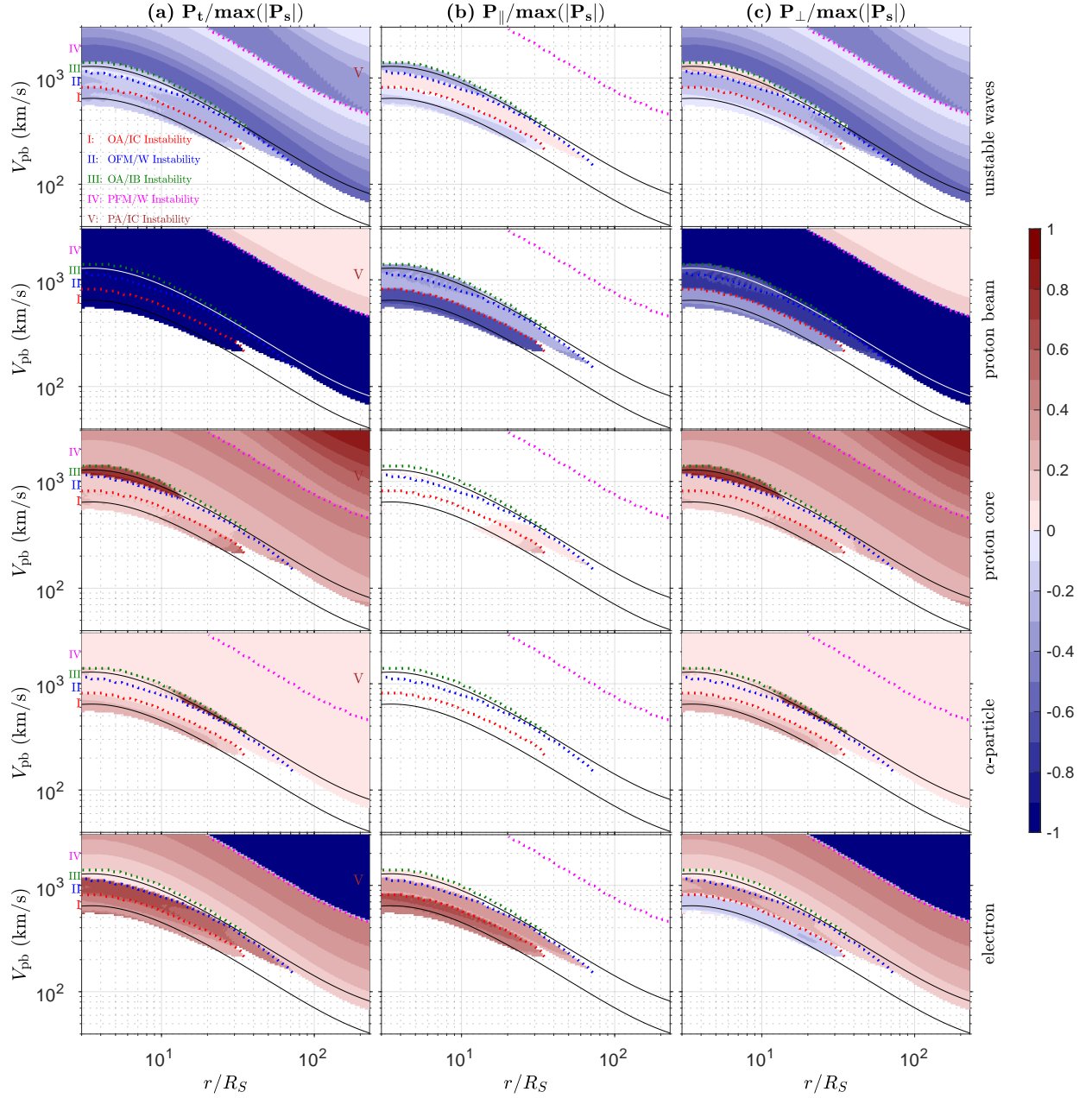


Figure 16. The $r - V_{pb}$ distributions of (a) total, (b) parallel, and (c) perpendicular energy transfer rate in proton beam instability. These energy transfer rates are normalized by $\max(|P_s|)$ which corresponds to energy flowing from the instability source particles into unstable waves, e.g., $\max(|P_s|) = |P_{pb}|$ in OA/IC, OFM/W, OA/IB, and PFM/W instabilities and $\max(|P_s|) = |P_e|$ in the PA/IC instability. The top panels give net energy transfer rates of unstable waves; and the second, third, fourth, and bottom panels present energy transfer rates associated with proton beam, proton core, alpha particle, and electron components, respectively. The regions controlled by OA/IC, OFM/W, OA/IB, PFM/W, and PA/IC instabilities are denoted by I, II, III, IV, and V, respectively. The boundary between two kinds of instabilities is denoted by dotted curves. Two solid curves represent $V_{pb} = V_A$ and $V_{pb} = 2V_A$, respectively. OA/IB = oblique Alfvén/ion-beam; OA/IC = oblique Alfvén/ion-cyclotron; OFM/W = oblique fast-magnetosonic/whistler; PA/IC = parallel Alfvén/ion-cyclotron; and PFM/W = parallel fast-magnetosonic/whistler.

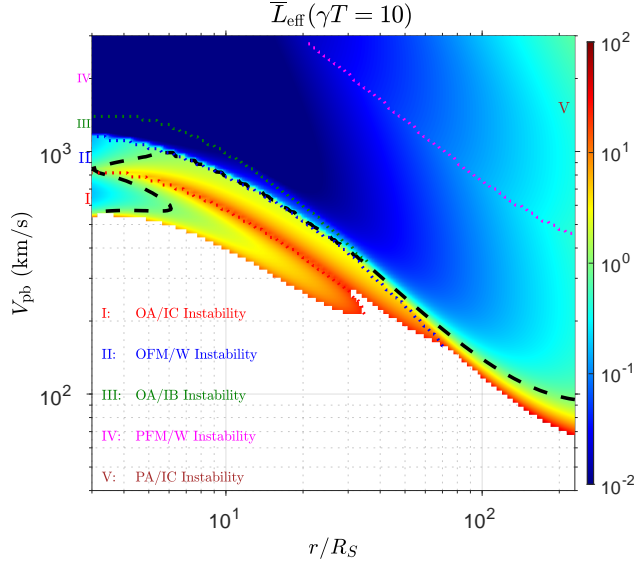


Figure 17. The $r - V_{\text{pb}}$ distribution of the normalized effective growth length $\bar{L}_{\text{eff}} = L_{\text{eff}}/R_S$. The dashed curve represents the counter line $\bar{L}_{\text{eff}} = 1$. The regions controlled by OA/IC, OFM/W, OA/IB, PFM/W, and PA/IC instabilities are denoted by I, II, III, IV, and V, respectively. The boundary between two kinds of instabilities is denoted by dotted curves. OA/IB = oblique Alfvén/ion-beam; OA/IC = oblique Alfvén/ion-cyclotron; OFM/W = oblique fast-magnetosonic/whistler; PA/IC = parallel Alfvén/ion-cyclotron; and PFM/W = parallel fast-magnetosonic/whistler.

Furthermore, under the assumption of constant V_{pb} , the growth length is estimated as

$$L_{\text{grow}} = (V_{\text{sw}} + V_{\text{pb}}) T_{\text{eff}} = (V_{\text{sw}} + V_{\text{pb}}) \times 10/\gamma. \quad (12)$$

In fact, due to a highly variable plasma and magnetic field in the inner heliosphere, the plasma environment cannot always be favorable of a continuous development of proton beam instability. Here, we assume the characteristic spatial scale corresponds to one solar radius in the highly variable plasma environment. As a result, the effective excitation would be estimated by using the normalized growth length defined as $\bar{L}_{\text{eff}} \equiv L_{\text{grow}}/R_S$. $\bar{L}_{\text{eff}} < 1$ corresponds to an effective excitation, whereas $\bar{L}_{\text{eff}} > 1$ corresponds to an ineffective excitation. The radial distribution of \bar{L}_{eff} is presented in Figure 17. It shows that oblique Alfvén/ion-cyclotron, oblique fast-magnetosonic/whistler and oblique Alfvén/ion-beam instabilities can be effectively excited by proton beams with $V_{\text{pb}} \sim 600 - 1300 \text{ km s}^{-1}$ in the $r \lesssim 6R_S$ solar atmosphere, and parallel fast-magnetosonic/whistler instability can be effectively driven by proton beams with $V_{\text{pb}} \gtrsim 2V_A$ in whole inner heliosphere.

6. DISCUSSION

6.1. Development of the plasma temperature anisotropy and its impact on proton beam instability

In this study, the plasma temperature is assumed to be isotropic for all particle species. Since energy transfer rates are different in the parallel and perpendicular directions, as shown in Figure 16 and Table 1 in Appendix B, this will result in different developments of parallel and perpendicular temperatures once the instability is triggered. Considering the energy transfer rates listed in Table 1 and assuming the energy totally responsible for the change in the plasma temperature, we can predict that:

(i) During oblique Alfvén/ion-cyclotron instability, due to $\bar{P}_{\text{pc}\perp} \simeq 0.20 \pm 0.03$ and $\bar{P}_{\text{pc}\parallel} \simeq 0.03 \pm 0.06$ for core protons, $T_{\text{pc}\perp}$ will become larger than $T_{\text{pc}\parallel}$. Similarly, $\bar{P}_{\alpha\perp} \simeq 0.19 \pm 0.06$ and $\bar{P}_{\alpha\parallel} \simeq 0$ will result in $T_{\alpha\perp}/T_{\alpha\parallel} > 1$. From $\bar{P}_{e\perp} \simeq -0.14 \pm 0.06$ and $\bar{P}_{e\parallel} \simeq 0.52 \pm 0.07$, this implies that $T_{e\perp}$ will decrease and $T_{e\parallel}$ will increase, inducing $T_{e\perp}/T_{e\parallel} < 1$.

(ii) During oblique fast-magnetosonic/whistler instability, $\bar{P}_{\text{pc}\perp} \simeq 0.16 \pm 0.03$ and $\bar{P}_{\text{pc}\parallel} \simeq 0.02 \pm 0.02$ will result in $T_{\text{pc}\perp}/T_{\text{pc}\parallel} > 1$. $\bar{P}_{\alpha\perp} \simeq 0.04 \pm 0.01$ and $\bar{P}_{\alpha\parallel} \simeq 0$ will induce $T_{\alpha\perp}$ slightly larger than $T_{\alpha\parallel}$. $\bar{P}_{e\perp} \simeq 0.25 \pm 0.07$ and $\bar{P}_{e\parallel} \simeq 0.32 \pm 0.02$ will cause $T_{e\perp}/T_{e\parallel} < 1$.

(iii) During oblique Alfvén/ion-beam instability, $T_{\text{pc}\perp}/T_{\text{pc}\parallel} > 1$ and $T_{\alpha\perp}/T_{\alpha\parallel} > 1$ will arise due to $\bar{P}_{\text{pc}\perp} \simeq 0.56 \pm 0.26$, $\bar{P}_{\text{pc}\parallel} \simeq 0$, $\bar{P}_{\alpha\perp} \simeq 0.23 \pm 0.23$ and $\bar{P}_{\alpha\parallel} \simeq 0$. However, $T_{e\perp}/T_{e\parallel}$ will be unchanged because of $\bar{P}_{e\perp} \simeq 0.02 \pm 0.01$ and $\bar{P}_{e\parallel} \simeq 0.03 \pm 0.02$.

(iv) During parallel fast-magnetosonic/whistler instability, $T_{\perp}/T_{\parallel} > 1$ will arise in the proton core, alpha particle, and electron populations due to $\bar{P}_{\text{pc}\perp} \simeq 0.33 \pm 0.06$, $\bar{P}_{\text{pc}\parallel} \simeq 0$, $\bar{P}_{\alpha\perp} \simeq 0.04 \pm 0.01$, $\bar{P}_{\alpha\parallel} \simeq 0$, $\bar{P}_{e\perp} \simeq 0.30 \pm 0.10$ and $\bar{P}_{e\parallel} \simeq 0$.

(v) During parallel Alfvén/ion-cyclotron instability, $T_{\perp}/T_{\parallel} > 1$ will arise in the proton beam, proton core, and alpha particle populations due to $\bar{P}_{\text{pb}\perp} \simeq 0.08 \pm 0.04$, $\bar{P}_{\text{pb}\parallel} \simeq 0$, $\bar{P}_{\text{pc}\perp} \simeq 0.54 \pm 0.16$, $\bar{P}_{\text{pc}\parallel} \simeq 0$, $\bar{P}_{\alpha\perp} \simeq 0.05 \pm 0.01$ and $\bar{P}_{\alpha\parallel} \simeq 0$.

The aforementioned predictions are performed for particle species that are not the source of each kind of instability. For the instability source particles, e.g., the proton beam in the first four instabilities and the electron beam population in the last instability, these particles will experience scattering by unstable waves along the velocity trajectory $(v_{\parallel} - v_{\text{ph}})^2 + v_{\perp}^2 = C$ in the wave frame, and the scattering of these particles can result in occurrence of the temperature anisotropy $T_{\perp}/T_{\parallel} > 1$. The development of $T_{\perp}/T_{\parallel} > 1$ of the proton beam

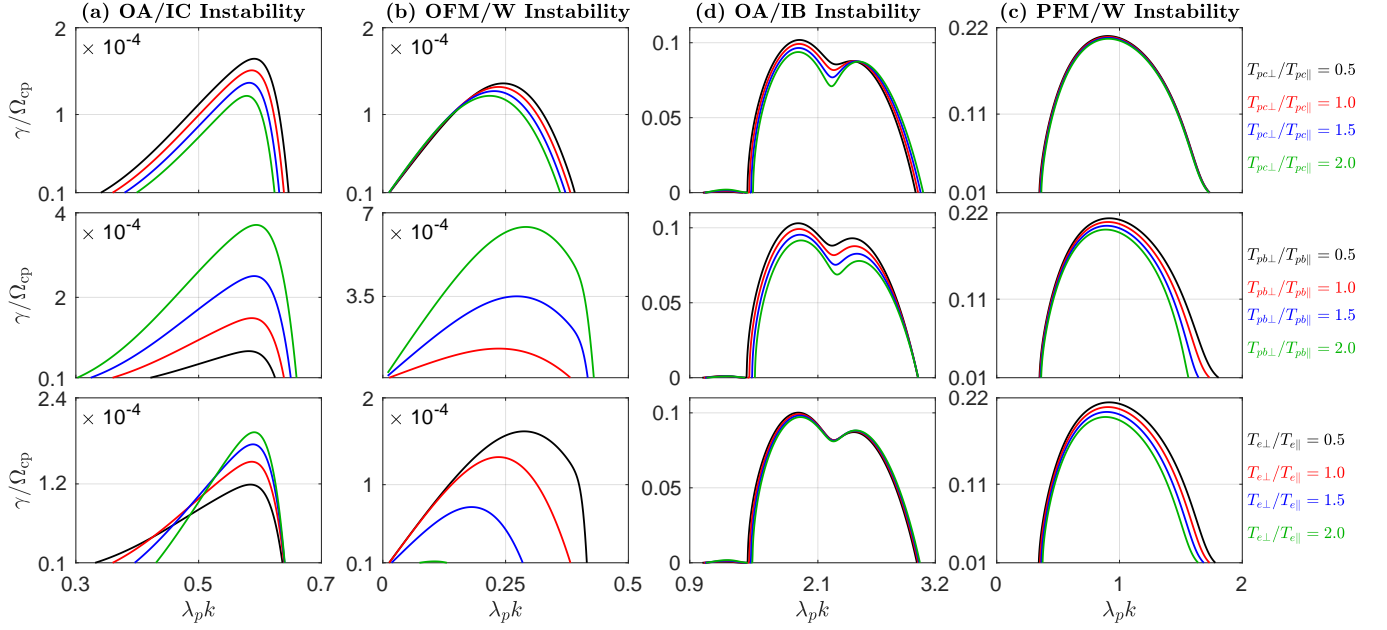


Figure 18. The dependence of the growth rate on the plasma temperature anisotropy in four typical proton beam instabilities at $r = 10R_S$ shown in Figure 3: (a) the OA/IC instability; (b) the OFM/W instability; (c) the OA/IB instability; and (d) the PFM/W instability. The top, middle, and bottom panels give the dependence on the temperature anisotropy of the proton core, proton beam, and electron components, respectively. The black, red, blue, and green curves denote $T_{\perp}/T_{\parallel} = 0.5, 1, 1.5$, and 2 , respectively. OA/IB = oblique Alfvén/ion-beam; OA/IC = oblique Alfvén/ion-cyclotron; OFM/W = oblique fast-magnetosonic/whistler; and PFM/W = parallel fast-magnetosonic/whistler.

has been identified in hybrid simulations of oblique Alfvén/ion-beam (Alfvén I) instability and parallel fast-magnetosonic/whistler instability (e.g., Daughton et al. 1999).

Actually, in situ satellites often detect anisotropic temperature in the solar wind plasma (e.g., Kasper et al. 2002; Hellinger et al. 2006; Klein et al. 2018; Huang et al. 2020). The statistical analysis further showed that the temperature anisotropy changes with heliocentric distance (e.g., Matteini et al. 2007). The wave-particle interactions during and after proton beam instability in the solar wind can provide one source of the temperature anisotropy distribution therein (Daughton et al. 1999; Hellinger & Trávníček 2011). We note there still exist other sources, e.g., adiabatic expansion and Coulomb collisions.

On the other hand, the temperature anisotropy will considerably affect proton beam instability (e.g., Montgomery et al. 1976; Daughton & Gary 1998; Sun et al. 2019; Xiang et al. 2020). Figure 18 exhibits the dependence of the four typical instabilities on $T_{pc\perp}/T_{pc\parallel}$, $T_{pb\perp}/T_{pb\parallel}$ and $T_{e\perp}/T_{e\parallel}$ in detail. This figure shows that the growth rate in oblique Alfvén/ion-cyclotron instability increases with increasing $T_{pb\perp}/T_{pb\parallel}$ and $T_{e\perp}/T_{e\parallel}$, and it decreases with increasing $T_{pc\perp}/T_{pc\parallel}$ before the temperature anisotropy instability is triggered (see also

Montgomery et al. 1976). For oblique Alfvén/ion-beam (Alfvén I) and parallel fast-magnetosonic/whistler instabilities, their growth rates decrease with increasing T_{\perp}/T_{\parallel} of the proton beam, proton core, and/or electron species (see also Daughton & Gary 1998). Besides, Figure 18 shows that the growth rate in oblique fast-magnetosonic/whistler instability decreases with increasing $T_{pc\perp}/T_{pc\parallel}$ and $T_{e\perp}/T_{e\parallel}$, and this growth rate increases with increasing $T_{pb\perp}/T_{pb\parallel}$.

6.2. Dependence of the alpha particle drift speed

In addition to the proton beam, alpha particles also flow faster than core protons in the solar wind (e.g., Marsch et al. 1982a). The differential drift between alpha and proton components can induce alpha particle beam instability (e.g., Verscharen & Chandran 2013; Liu et al. 2019). To show the difference between proton beam instability and alpha particle beam instability, Figure 19 presents the $V_{\alpha} - \theta$ distributions of the instability driven by alpha particle beams at three heliocentric distances, $r = 10R_S$, $55R_S$ and $100R_S$. There are three typical instabilities at $r = 10R_S$: Alfvén/ion-cyclotron instability, oblique Alfvén/ion-beam instability, and parallel fast-magnetosonic/whistler instability. Also, oblique Alfvén/ion-beam instability arises at low V_{α}/V_A in comparison with the same kind of instability

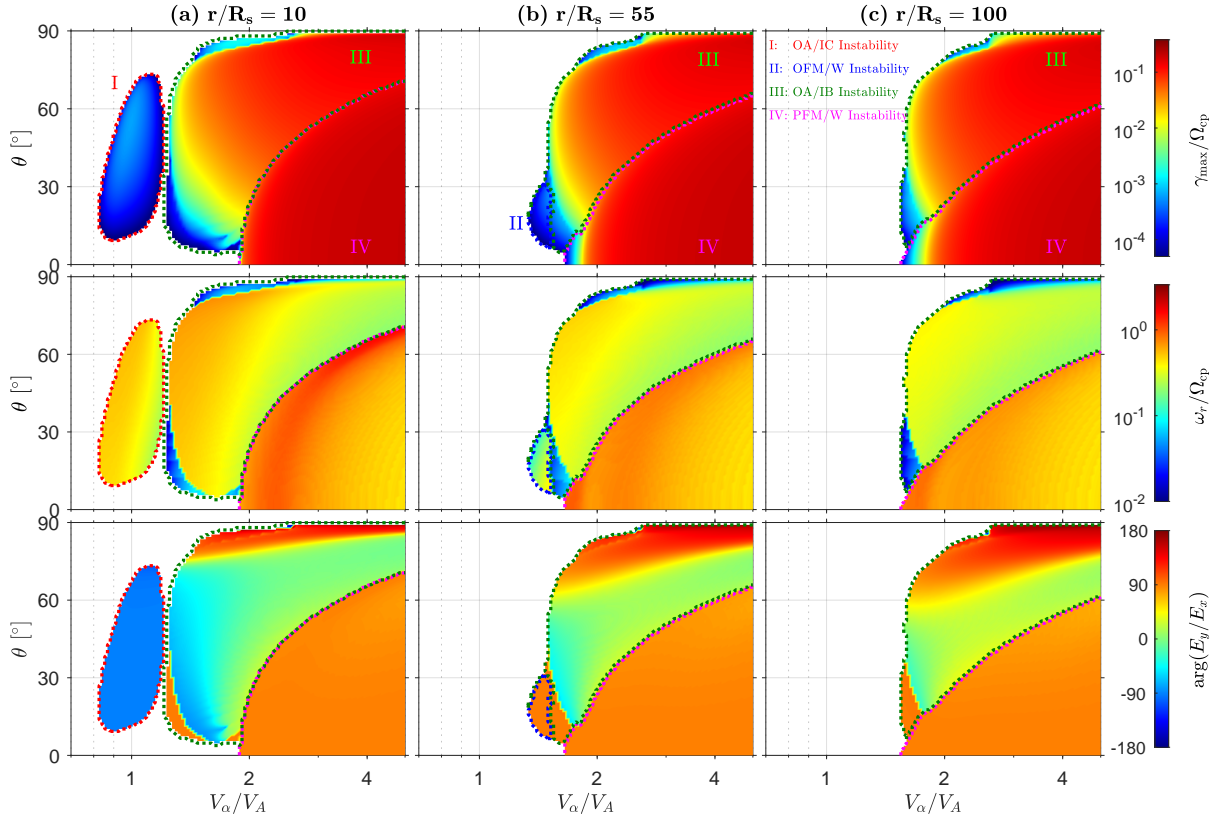


Figure 19. The $V_\alpha - \theta$ distributions of the alpha particle beam instability at (a) $r = 10R_S$, (b) $r = 55R_S$, and (c) $r = 100R_S$. (Top panels) the maximum growth rate, γ_{\max} ; (second panels) the real frequency ω_r at γ_{\max} ; and (bottom panels) the argument of E_y/E_x at γ_{\max} . The regions controlled by OA/IC, OFM/W, OA/IB, and PFM/W instabilities are denoted by I, II, III, and IV, respectively. OA/IB = oblique Alfvén/ion-beam; OA/IC = oblique Alfvén/ion-cyclotron; OFM/W = oblique fast-magnetosonic/whistler; and PFM/W = parallel fast-magnetosonic/whistler.

driven by the proton beam (see Figure 14). The detailed differences among different ion beam instabilities will be studied in the future.

6.3. Dependence of the proton beam density

Proton beam instability is strongly dependent on the relative density of the proton beam (e.g., [Montgomery et al. 1976](#)). In order to show a comprehensive overview, the $V_{pb} - \theta$ distributions of proton beam instability with four relative beam densities $n_{pb} = 0.05n_e$, $0.1n_e$, $0.25n_e$, and $0.45n_e$ are presented in Figure 20, which exhibits the dependence of proton beam instability on n_{pb}/n_e at $r = 10R_S$. When n_{pb}/n_e increases, the characteristic features in each instability are that: (1) the maximum growth rate in oblique Alfvén/ion-cyclotron instability arises at larger θ ; (2) oblique fast-magnetosonic/whistler instability is controlled by oblique Alfvén/ion-cyclotron instability or by oblique Alfvén/ion-beam instability; (3) oblique Alfvén/ion-beam instability becomes dominant at smaller V_{pb}/V_A ; and (4) the instability threshold of parallel fast-magnetosonic/whistler instability moves to larger V_{pb}/V_A . These changes also occur at other he-

liocentric distances. It should be noted that although oblique Alfvén/ion-cyclotron instability is quenched at $r = 55R_S$ and $100R_S$ in Figure 14 where $n_{pb}/n_e = 0.1$, this instability can be driven by the proton beam with larger n_{pb}/n_e , and the reason is that large n_{pb}/n_e provides more free energy for amplification of the instability, and small n_{pc}/n_e absorbs less energy from unstable waves (leading to weak damping).

Moreover, for a specific case, i.e., oblique Alfvén/ion-cyclotron instability at $V_{pb} = V_A$ in low-beta plasma, the growth rate always increases with the relative beam density, which is consistent with results given in [Montgomery et al. \(1976\)](#). For oblique Alfvén/ion-beam instability and parallel fast-magnetosonic/whistler instability at $V_{pb} = 2V_A$, their growth rates are first enhancing and then reducing as the relative proton beam density increases, and these two instabilities are even quenched at large relative beam densities ([Montgomery et al. 1976](#); [Daughton & Gary 1998](#)).

From Figure 20, we can see that proton beam instability are sensitive on n_{pb}/n_e . If we consider the value of n_{pb}/n_e different from $n_{pb}/n_e = 0.1$, the radial distribu-

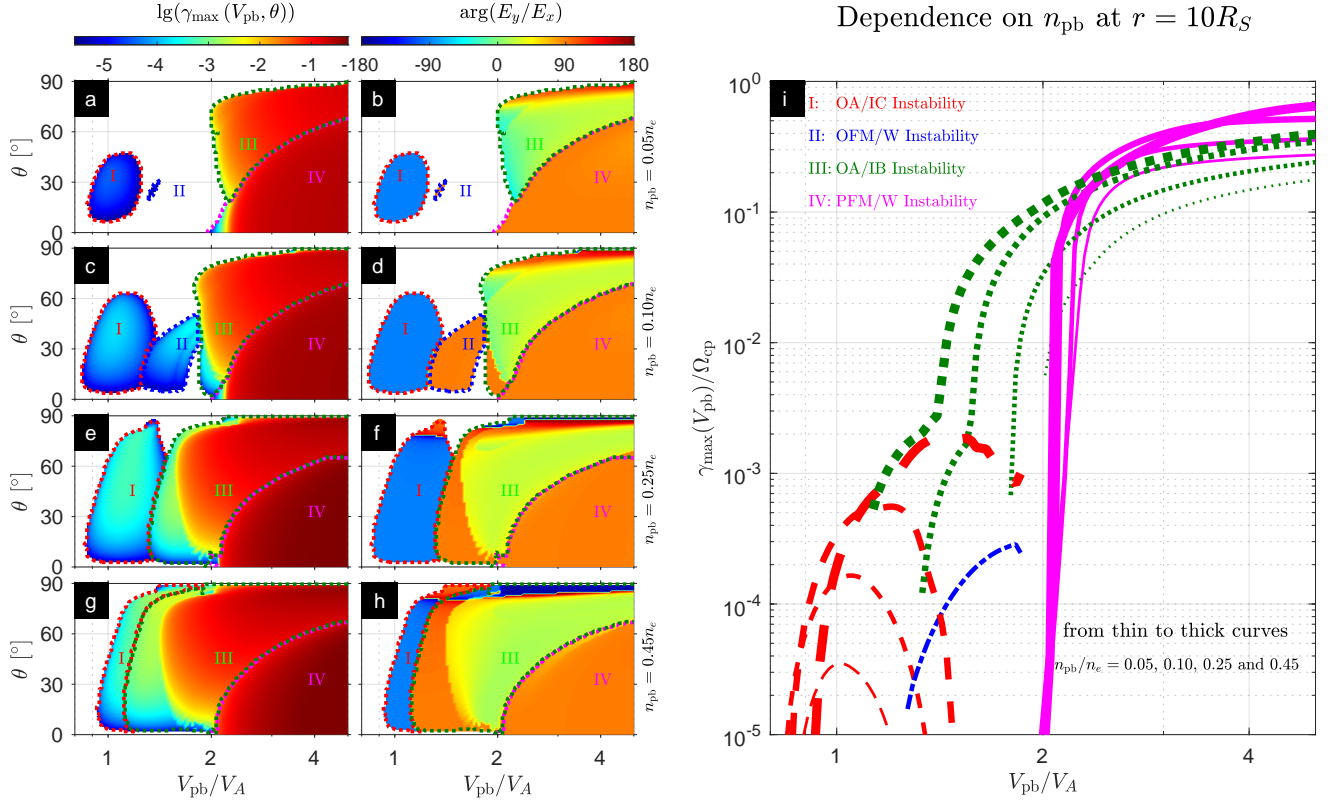


Figure 20. The dependence of proton beam instability on n_{pb} at $r = 10R_s$: (a)–(b) $n_{pb} = 0.05n_e$; (c)–(d) $n_{pb} = 0.10n_e$; (e)–(f) $n_{pb} = 0.25n_e$; and (g)–(h) $n_{pb} = 0.45n_e$. Panel (i) presents one-dimensional distribution of the maximum growth rate γ_{\max} as a function of V_{pb} . The dashed, dashed-dotted, dotted, and solid curves represent OA/IC, OFM/W, OA/IB, and PFM/W instabilities, respectively. OA/IB = oblique Alfvén/ion-beam; OA/IC = oblique Alfvén/ion-cyclotron; OFM/W = oblique fast-magnetosonic/whistler; and PFM/W = parallel fast-magnetosonic/whistler.

tion of proton beam instability would be different from that shown in Figure 15. However, the basic features are qualitatively consistent with that shown in Figures 15. Recently, Verniero et al. (2020) found that n_{pb}/n_{pc} can be larger than 1 at $r \simeq 36R_s$, and this is more in favor of the excitation of proton beam instability in the inner heliosphere.

6.4. Observational evidence of proton beam instability

Since proton beam instability is widely thought of strongly constraining the proton beam in the solar-terrestrial environments, both statistical and case studies try to provide the observational evidence of the excitation of the instability (e.g., Dum et al. 1980; Leubner & Vinas 1986; Marsch & Livi 1987; Goldstein et al. 2000; Gary et al. 2016; Zhao et al. 2019; Verniero et al. 2020). The statistical studies of Marsch & Livi (1987) and Goldstein et al. (2000) analyzed the $V_{pb} - n_{pb}$ distributions using Helios and Ulysses data, and they concluded that the beam instability constrains the proton beam speed in the solar wind. However, Tu et al. (2004) found a weak correlation between Alfvén I insta-

bility and the observed data set in the $V_{pb} - \beta_{pc}$ distribution. Because Tu et al. (2004) used the theoretical predictions of the Alfvén I instability under limited parameters (Daughton & Gary 1998), the robust relation between the data set given by Tu et al. (2004) and the theoretical results under the actual plasma parameters is still unclear. Klein et al. (2018) statistically studied the ion kinetic instability for 309 randomly selected events through Nyquist’s instability criterion, and they found that a majority of the ion instabilities occur in the presence of a proton beam (also see Klein et al. 2019).

On the other hand, from case studies, the occurrence of proton beam instability is identified by previous works (e.g., Dum et al. 1980; Leubner & Vinas 1986; Gary et al. 2016; Zhao et al. 2019; Verniero et al. 2020; Klein et al. 2021). In particular, using PSP measurements, Verniero et al. (2020) found coexistence of ion-scale waves and ion beams at $r \sim 40R_s$, and they identified the appearance of both parallel Alfvén/ion-cyclotron and fast-magnetosonic/whistler instabilities. Furthermore, Zhao et al. (2019) identified the interplay of proton beam and proton temperature anisotropy on proton insta-

bility, and they provided an observational evidence of proton instability enhanced by the proton beam. Recently, Klein et al. (2021) used two popular models (a single anisotropic population and two relatively drifting anisotropic populations) to fit the proton phase-space densities in two ion-scale wave activity events observed by PSP, and they found that the two-component model can result in instability much stronger than the one-component model.

The aforementioned works mainly checked the observations to the theoretical predictions of parallel fast-magnetosonic/whistler instability and oblique Alfvén/ion-beam (Alfvén I) instability. In this study, we propose that oblique Alfvén/ion-cyclotron instability and oblique fast-magnetosonic/whistler instability can be effectively excited in the solar atmosphere, which can be checked by using PSP measurements.

In addition to the resonant proton beam instabilities, a sufficiently dense and/or fast proton beam can provide sufficient excess parallel pressure to destabilize the CGL firehose instability (e.g., Kunz et al. 2015). The instability condition is $\Lambda_f = \Sigma_s (\beta_{s\parallel} - \beta_{s\perp})/2 + \Sigma_s (n_s m_s V_s^2) / \Sigma_s (n_s m_s V_A^2) > 1$ (e.g., Kunz et al. 2015; Chen et al. 2016), which yields a relation of $V_{pb} \gtrsim \sqrt{n_e/n_{pb}} V_A \simeq 4.5 V_A$ in the plasma with isotropic temperatures. However, in situ observations show that the proton beam with $V_{pb} \gtrsim 4.5 V_A$ may only exist upstream of the interplanetary shocks in the solar wind (e.g., Kadić et al. 2017).

7. SUMMARY

This paper presents a comprehensive investigation of the energy transfer rate, radial distribution, and effective excitation of proton beam instability in the inner heliosphere.

We firstly analyzed the nature and excitation mechanism of the four typical proton beam instabilities in Section 3, i.e., oblique Alfvén/ion-cyclotron instability, oblique fast-magnetosonic/whistler instability, oblique Alfvén/ion-beam instability, and parallel fast-magnetosonic/whistler instability. In particular, we find oblique Alfvén/ion-beam instability can be classified into three types (Figures 10 and 11), and the wave mode in these three types corresponds to the long-wavelength branch of the Alfvén/ion-beam mode wave (Type-I), the coupling mode between the Alfvén/ion-beam mode and the Alfvén/ion-cyclotron mode (Type-II) and the coupling mode between the Alfvén/ion-beam mode and the alpha cyclotron mode (or the Alfvén/ion-beam mode wave at $\omega_r \gtrsim \Omega_{c\alpha}$; Type-III).

Based on the energy transfer rate and the diffusive particle flux path, we further clarified the roles

of wave-particle resonant interactions on the instability excitation. Oblique Alfvén/ion-cyclotron instability is mainly triggered by Landau and transit-time interactions with $n = 0$ resonant beam protons. Oblique fast-magnetosonic/whistler instability is produced through Landau and transit-time interactions with $n = 0$ resonant beam protons and cyclotron interactions with $n = -1$ resonant beam protons. For oblique Alfvén/ion-beam instability, its excitation mechanisms include cyclotron interactions with $n = -1$ resonant beam protons and with $n = 1$ resonant electrons as well as wave-particle interactions of these resonant particles resulting from the parallel electric field. In addition, parallel fast-magnetosonic/whistler instability is induced by the $n = -1$ cyclotron resonant interactions with beam protons.

Secondly, from the radial distribution of proton beam instability in the inner heliosphere, we exhibited the possible excitation region for each instability, i.e., the region with $V_{pb} \sim 0.8 - 1.4 V_A$ and $r \lesssim 30 R_S$ for oblique Alfvén/ion-cyclotron instability, the region with $V_{pb} \sim 1.3 - 2 V_A$ and $r \lesssim 60 R_S$ for oblique fast-magnetosonic/whistler instability, the region with $V_{pb} \sim 1.7 - 2.2 V_A$ and $r \lesssim 30 R_S$ for oblique Alfvén/ion-beam instability, and parallel fast-magnetosonic/whistler instability controlling the whole inner heliosphere as $V_{pb} \sim 1.6 - 11 V_A$. It is evident that proton beam instability can provide a strong constraint on the proton beam speed in the inner heliosphere. We also exhibited the radial distributions of the energy transfer rate in these instabilities, which provide strong implications on different changes of plasma parallel and perpendicular temperatures in the inner heliosphere (see discussion in Subsection 6.1).

Furthermore, we proposed an effective excitation length to estimate the sufficient growth of proton beam instability in the inner heliosphere. In particular, we showed that oblique Alfvén/ion-cyclotron instability, oblique fast-magnetosonic/whistler instability and oblique Alfvén/ion-beam instability can be effectively excited by beam protons with the drift speed of $\sim 600 - 1300 \text{ km s}^{-1}$. Since oblique Alfvén/ion-cyclotron and Alfvén/ion-beam waves can be significantly damped in the solar atmosphere, oblique Alfvén/ion-cyclotron instability and oblique Alfvén/ion-beam instability can contribute to the solar coronal heating during and after the instability.

Lastly, this study shows the dependence of proton beam instability on the plasma parameters, such as the plasma temperature anisotropy, the drift speed of the alpha particles, and the relative density of the proton beam (see Figures 18–20). Although proton beam in-

stability is indeed sensitive to these plasma parameters, our results explored the basic features of such instability.

This work was supported by the NNSFC grant Nos. 41974203, 41531071, and 11673069. The author J.Z. appreciates the referee for helpful suggestions and inspiring comments.

APPENDIX

A. SEVERAL EXPRESSIONS OF THE ENERGY TRANSFER RATE

From Ampere's and Faraday's laws in Fourier space,

$$\mathbf{k} \times \mathbf{B} = -i\mu_0 \mathbf{J} - \frac{\omega \mathbf{E}}{c^2}, \quad (\text{A1})$$

$$\mathbf{k} \times \mathbf{E} = \omega \mathbf{B}, \quad (\text{A2})$$

the total energy transfer rate can be given as

$$P_t = \frac{\mathbf{E} \cdot \mathbf{J}^* + \mathbf{E}^* \cdot \mathbf{J}}{4W_{\text{EB}}} = -2\gamma, \quad (\text{A3})$$

which clearly indicates that P_t and γ have reversed energy flow directions.

In order to illustrate the difference between our expression of the energy transfer rate and the expression proposed in previous studies (e.g., Quataert 1998), we rewrite P_s in terms of the susceptibility tensor χ_s using $\sigma_s = -i\epsilon_0\omega\chi_s$ and $\omega = \omega_r + i\gamma$,

$$P_s = \omega_r \frac{\epsilon_0 \mathbf{E}^* \cdot \chi_{sa} \cdot \mathbf{E}}{2W_{\text{EB}}} + \gamma \frac{\epsilon_0 \mathbf{E}^* \cdot \chi_{sh} \cdot \mathbf{E}}{2W_{\text{EB}}}, \quad (\text{A4})$$

where $\chi_{sh} = (\chi_s + \chi_s^\dagger)/2$ and $\chi_{sa} = (\chi_s - \chi_s^\dagger)/2i$ denote the Hermitian and anti-Hermitian parts of χ_s , respectively. Under the assumption of $\omega_r \gg \gamma$, Equation (A4) can be reduced to the following expression at the condition of $\mathbf{E}^* \cdot \chi_{sa} \cdot \mathbf{E} \gtrsim \mathbf{E}^* \cdot \chi_{sh} \cdot \mathbf{E}$,

$$P_s \simeq \omega_r \frac{\epsilon_0 \mathbf{E}^* \cdot \chi_{sa} \cdot \mathbf{E}}{2W_{\text{EB}}}. \quad (\text{A5})$$

Different from expressions (A4) and (A5), previous studies often use the energy transfer defined by Quataert (1998)

$$P_s^Q \equiv \frac{\mathbf{E}^* \cdot \chi_{sa} \cdot \mathbf{E}}{4W_{\text{EB}}} [\text{CGS}] = \frac{\pi\epsilon_0 \mathbf{E}^* \cdot \chi_{sa} \cdot \mathbf{E}}{W_{\text{EB}}} [\text{SI}], \quad (\text{A6})$$

where χ_{sa} is calculated under the assumption of $\omega = \omega_r$. Through Equations (A3) and (A5), we have

$$\Sigma_s P_s^Q \simeq -\frac{4\pi\gamma}{\omega_r} = -2\gamma T, \quad (\text{A7})$$

where $T = 2\pi/\omega_r$ is the wave period. P_s^Q describes the energy transfer per unit of volume and per unit of wave energy in one mode period (Quataert 1998).

Comparing expressions (A4)–(A6), we can see that expression (A6) is valid under the condition $\gamma \ll \omega_r$. This implies that expression (A6) cannot describe the energy transfer associated with plasma waves with zero real frequency, for example, unstable waves driven by oblique firehose instability and ion/electron mirror instability (e.g., Sun et al. 2019, 2020). Although our expressions (e.g., expressions (6), (7), (A4), (A5)) and Quataert's expression (A6) have slightly different physical meanings, they are all helpful in quantifying the energy transfer between waves and particles.

B. TYPICAL PARAMETERS OF PROTON BEAM INSTABILITY

Based on the data in Figures 15 and 16, Table 1 summarizes characteristic values of the typical parameters in different proton beam instabilities. This table is helpful for understanding the evolution of proton beam instability in the inner heliosphere. For example, Subsection 6.1 discusses the evolution of both parallel and perpendicular plasma temperatures according to the energy transfer rates listed in Table 1.

Table 1. Typical parameters of proton beam instability[†]

	OA/IC	OFM/W	OA/IB	PFM/W	PA/IC
r/R_S	$\lesssim 30$	$\lesssim 60$	$\lesssim 30$	no limitation	no limitation
V_{pb}/V_A	$0.8 - 1.4$	$1.3 - 2.0$	$1.7 - 2.2$	$1.6 - 11$	$\gtrsim 11$
γ/Ω_{cp}	$\sim 1.2 \times 10^{-4}$	$\sim 3.4 \times 10^{-4}$	$\sim 3.2 \times 10^{-2}$	~ 0.3	~ 0.7
ω_r/Ω_{cp}	~ 0.30	~ 0.25	~ 0.59	~ 0.84	~ 0.52
$\arg(E_y/E_x)$	-90°	90°	$\sim 11^\circ$	90°	-90°
$ E_y/E_x $	0.42 ± 0.15	1.55 ± 0.14	0.07 ± 0.03	1	1
$\lambda_p k$	0.47 ± 0.06	0.23 ± 0.07	2.15 ± 0.62	0.46 ± 0.21	0.63 ± 0.13
θ	$38^\circ \pm 7^\circ$	$34^\circ \pm 6^\circ$	$68^\circ \pm 6^\circ$	0°	0°
\bar{P}_{pb}	-1	-1	-1	-1	0.08 ± 0.04
$\bar{P}_{pb\perp}$	-0.36 ± 0.04	-0.71 ± 0.01	-0.72 ± 0.07	-1	0.08 ± 0.04
$\bar{P}_{pb\parallel}$	-0.64 ± 0.04	-0.29 ± 0.01	-0.28 ± 0.07	0	0
\bar{P}_{pc}	0.23 ± 0.08	0.17 ± 0.05	0.56 ± 0.27	0.33 ± 0.07	0.54 ± 0.16
$\bar{P}_{pc\perp}$	0.20 ± 0.03	0.16 ± 0.03	0.56 ± 0.26	0.33 ± 0.06	0.54 ± 0.16
$\bar{P}_{pc\parallel}$	0.03 ± 0.06	0.02 ± 0.02	0	0	0
\bar{P}_α	0.19 ± 0.06	0.04 ± 0.01	0.23 ± 0.23	0.04 ± 0.01	0.05 ± 0.01
$\bar{P}_{\alpha\perp}$	0.19 ± 0.06	0.04 ± 0.01	0.23 ± 0.23	0.04 ± 0.01	0.05 ± 0.01
$\bar{P}_{\alpha\parallel}$	< 0.001	< 0.001	~ 0.001	0	0
\bar{P}_e	0.38 ± 0.08	0.57 ± 0.08	0.05 ± 0.02	0.30 ± 0.10	-1
$\bar{P}_{e\perp}$	-0.14 ± 0.06	0.25 ± 0.07	0.02 ± 0.01	0.30 ± 0.10	-1
$\bar{P}_{e\parallel}$	0.52 ± 0.07	0.32 ± 0.02	0.03 ± 0.02	0	0
\bar{P}_t	-0.20 ± 0.03	-0.22 ± 0.04	-0.16 ± 0.09	-0.34 ± 0.17	-0.33 ± 0.12
$\bar{P}_{t\perp}$	-0.11 ± 0.04	-0.26 ± 0.04	0.08 ± 0.13	-0.34 ± 0.17	-0.33 ± 0.12
$\bar{P}_{t\parallel}$	-0.09 ± 0.04	0.04 ± 0.01	-0.24 ± 0.05	0	0

NOTE—[†] \bar{P} is defined as $\bar{P} \equiv P/\max(|P_s|)$, where $\max(|P_s|)$ is the magnitude of the energy transfer rate between unstable waves and instability source particles that provide free energy to trigger the instability. $|E_y/E_x|$, $\lambda_p k$, θ and \bar{P} are given by using the mean and the standard deviation.

REFERENCES

- Alterman, B. L., Kasper, J. C., Stevens, M. L., et al. 2018, ApJ, 864, 112. doi:10.3847/1538-4357/aad23f
- Bale, S. D., Goetz, K., Harvey, P. R., et al. 2016, SSRv, 204, 49. doi:10.1007/s11214-016-0244-5
- Bowen, T. A., Mallet, A., Huang, J., et al. 2020, ApJS, 246, 66. doi:10.3847/1538-4365/ab6c65
- Chen, C. H. K., Matteini, L., Schekochihin, A. A., et al. 2016, ApJL, 825, L26. doi:10.3847/2041-8205/825/2/L26
- Daughton, W. & Gary, S. P. 1998, J. Geophys. Res., 103, 20613. doi:10.1029/98JA01385
- Daughton, W., Gary, S. P., & Winske, D. 1999, J. Geophys. Res., 104, 4657. doi:10.1029/1998JA900105
- Dum, C. T., Marsch, E., & Pilipp, W. 1980, JPIPh, 23, 91. doi:10.1017/S0022377800022170
- Đurovcová, T., Šafránková, J., & Němeček, Z. 2019, SoPh, 294, 97. doi:10.1007/s11207-019-1490-y
- Feldman, W. C., Asbridge, J. R., Bame, S. J., et al. 1973, J. Geophys. Res., 78, 2017. doi:10.1029/JA078i013p02017
- Feldman, W. C., Asbridge, J. R., Bame, S. J., et al. 1974, Reviews of Geophysics and Space Physics, 12, 715. doi:10.1029/RG012i004p00715
- Gary, S. P. 1991, SSRv, 56, 373. doi:10.1007/BF00196632
- Gary, S. P., Jian, L. K., Broiles, T. W., et al. 2016, J. Geophys. Res., 121, 30. doi:10.1002/2015JA021935
- Goldstein, B. E., Neugebauer, M., Zhang, L. D., et al. 2000, Geophys. Res. Lett., 27, 53. doi:10.1029/1999GL003637
- He, J., Zhu, X., Verscharen, D., et al. 2020, ApJ, 898, 43. doi:10.3847/1538-4357/ab9174
- Hellinger, P., Trávníček, P., Kasper, J. C., et al. 2006, Geophys. Res. Lett., 33, L09101. doi:10.1029/2006GL025925

- Hellinger, P. & Trávníček, P. M. 2011, *J. Geophys. Res.*, 116, A11101. doi:10.1029/2011JA016940
- Howes, G. G., Klein, K. G., & Li, T. C. 2017, *Journal of Plasma Physics*, 83, 705830102. doi:10.1017/S0022377816001197
- Huang, J., Kasper, J. C., Vech, D., et al. 2020, *ApJS*, 246, 70. doi:10.3847/1538-4365/ab74e0
- Kajdič, P., Hietala, H., & Blanco-Cano, X. 2017, *ApJL*, 849, L27. doi:10.3847/2041-8213/aa94c6
- Kasper, J. C., Lazarus, A. J., & Gary, S. P. 2002, *Geophys. Res. Lett.*, 29, 1839. doi:10.1029/2002GL015128
- Kennel, C. F. & Engelmann, F. 1966, *PhFl*, 9, 2377. doi:10.1063/1.1761629
- Klein, K. G., Howes, G. G., & Tenbarger, J. M. 2017, *Journal of Plasma Physics*, 83, 535830401. doi:10.1017/S0022377817000056
- Klein, K. G., Alterman, B. L., Stevens, M. L., et al. 2018, *PhRvL*, 120, 205102. doi:10.1103/PhysRevLett.120.205102
- Klein, K. G., Martinović, M., Stansby, D., et al. 2019, *ApJ*, 887, 234. doi:10.3847/1538-4357/ab5802
- Klein, K. G., Howes, G. G., TenBarge, J. M., et al. 2020, *Journal of Plasma Physics*, 86, 905860402. doi:10.1017/S0022377820000689
- Klein, K. G., Verniero, J. L., Alterman, B., et al. 2021, *ApJ*, 909, 7. doi:10.3847/1538-4357/abd7a0
- Kunz, M. W., Schekochihin, A. A., Chen, C. H. K., et al. 2015, *Journal of Plasma Physics*, 81, 325810501. doi:10.1017/S0022377815000811
- Leubner, M. P. & Vinas, A. F. 1986, *J. Geophys. Res.*, 91, 13366. doi:10.1029/JA091iA12p13366
- Liu, Z., Zhao, J., Sun, H., et al. 2019, *ApJ*, 874, 128. doi:10.3847/1538-4357/ab0896
- Marsch, E. & Livi, S. 1987, *J. Geophys. Res.*, 92, 7263. doi:10.1029/JA092iA07p07263
- Marsch, E., Rosenbauer, H., Schwenn, R., et al. 1982, *J. Geophys. Res.*, 87, 35. doi:10.1029/JA087iA01p00035
- Marsch, E., Schwenn, R., Rosenbauer, H., et al. 1982, *J. Geophys. Res.*, 87, 52. doi:10.1029/JA087iA01p00052
- Matteini, L., Landi, S., Hellinger, P., et al. 2007, *Geophys. Res. Lett.*, 34, L20105. doi:10.1029/2007GL030920
- Montgomery, M. D., Gary, S. P., Forslund, D. W., et al. 1975, *PhRvL*, 35, 667. doi:10.1103/PhysRevLett.35.667
- Montgomery, M. D., Gary, S. P., Feldman, W. C., et al. 1976, *J. Geophys. Res.*, 81, 2743. doi:10.1029/JA081i016p02743
- Quataert, E. 1998, *ApJ*, 500, 978. doi:10.1086/305770
- Sun, H., Zhao, J., Xie, H., et al. 2019, *ApJ*, 884, 44. doi:10.3847/1538-4357/ab3dad
- Sun, H., Zhao, J., Liu, W., et al. 2020, *ApJ*, 902, 59. doi:10.3847/1538-4357/abb3ca
- Stix, T. H. 1992, *Waves in plasmas*, by Stix, Thomas Howard.; Stix, Thomas Howard. New York : American Institute of Physics, c1992.
- Sittler, E. C. & Guhathakurta, M. 1999, *ApJ*, 523, 812. doi:10.1086/307742
- Tu, C.-Y., Marsch, E., & Qin, Z.-R. 2004, *J. Geophys. Res.*, 109, A05101. doi:10.1029/2004JA010391
- Verniero, J. L., Larson, D. E., Livi, R., et al. 2020, *ApJS*, 248, 5. doi:10.3847/1538-4365/ab86af
- Verscharen, D. & Chandran, B. D. G. 2013, *ApJ*, 764, 88. doi:10.1088/0004-637X/764/1/88
- Winske, D. & Omid, N. 1992, *J. Geophys. Res.*, 97, 14779. doi:10.1029/92JA00902
- Xiang, L., Lee, K. H., Wu, D. J., Lee, L. C. 2020, *ApJ*, 899, 61. doi:10.3847/1538-4357/ab9f9a
- Xie, H. 2019, *CoPhC*, 244, 343. doi:10.1016/j.cpc.2019.06.014
- Xie, H. & Xiao, Y. 2016, *PIST*, 18, 97. doi:10.1088/1009-0630/18/2/01
- Zhao, J., Wang, T., Shi, C., et al. 2019, *ApJ*, 883, 185. doi:10.3847/1538-4357/ab3bd1